MIT Libraries | DSpace@MIT

MIT Open Access Articles

Contributed Review: Experimental characterization of inverse piezoelectric strain in GaN HEMTs via micro-Raman spectroscopy

Massachusetts Institute of Technology

Experimental characterization of inverse piezoelectric strain in GaN HEMTs via micro-Raman spectroscopy

Kevin R. Bagnall and Evelyn N. Wang

Department of Mechanical Engineering, Massachusetts Institute of Technology, Cambridge, Massachusetts, 02139, USA

Micro-Raman thermography is one of the most popular techniques for measuring local temperature rise in gallium nitride (GaN) high electron mobility transistors (HEMTs) with high spatial and temporal resolution. However, accurate temperature measurements based on changes in the Stokes peak positions of the GaN epitaxial layers requires properly accounting for the stress and/or strain induced by the inverse piezoelectric effect. It is common practice to use the pinched OFF state as the unpowered reference for temperature measurements because the vertical electric field in the GaN buffer that induces inverse piezoelectric stress/strain is relatively independent of the gate bias. Although this approach has yielded temperature measurements that agree with those derived from the Stokes/anti-Stokes ratio and thermal models, there has been significant difficulty in quantifying the mechanical state of the GaN buffer in the pinched OFF state from changes in the Raman spectra. In this paper, we review the experimental technique of micro-Raman thermography and derive expressions for the detailed dependence of the Raman peak positions on strain, stress, and electric field components in wurtzite GaN. We also use a combination of semiconductor device modeling and electro-mechanical modeling to predict the stress and strain induced by the inverse piezoelectric effect. Based on the insights gained from our electro-mechanical model and the best values of material properties in the literature, we analyze changes in the E_2 high and A_1 (LO) Raman peaks and demonstrate that there are major quantitative discrepancies between measured and modeled values of inverse piezoelectric stress and strain. We examine many of the hypotheses offered in the literature for these discrepancies but conclude that

1

none of them satisfactorily resolves these discrepancies. Further research is needed to determine whether the electric field along the c-axis could be affecting the phonon frequencies apart from the inverse piezoelectric effect in wurtzite GaN, which has been predicted theoretically in zinc blende gallium arsenide (GaAs).

I. Introduction

Due to the excellent electrical properties of gallium nitride (GaN), GaN-based high electron mobility transistors (HEMTs) are one most promising semiconductor technologies for high power, high frequency defense and commercial wireless communications applications [1]. However, the high dissipated power densities present in GaN power amplifiers (PAs) can lead to high channel temperatures and degraded performance and reliability. Over the last ten years, micro-Raman spectroscopy has become one of the most popular techniques for measuring local temperature rise in GaN HEMTs owing to its high spatial resolution of ≈1 µm and the wide availability of commercial micro-Raman systems [2]-[9]. The temperature of the GaN epitaxial layer(s) of interest is typically measured by either the change in center position or linewidth of the Stokes peak or the ratio of the intensities of the Stokes to anti-Stokes peaks. Although the Stokes/anti-Stokes ratio technique is theoretically more ideal for temperature measurements because it is not affected by mechanical stress or strain, the Stokes peak position technique is more popular because of the longer acquisition time and more expensive optical filters required for Stokes/anti-Stokes measurements [4],[9]. It has also been suggested that the non-equilibrium distribution of hot phonons emitted by electron-phonon scattering in GaN HEMTs could lead to erroneous temperature measurements using the Stokes/anti-Stokes ratio of the A_1 (LO) mode [10].

The earliest reports of micro-Raman thermography in GaN HEMTs utilized an empirical formula fitted to experimental data to relate the Stokes line position to the GaN temperature [2],[11]. Over time, it has been recognized that the inverse piezoelectric (IPE) and thermoelastic effects may also change the Stokes line position when a GaN HEMT is biased in the ON state, which needs to be accounted for in order to accurately measure the device temperature [4],[7]-[9],[12]. Sarua $et\ al.$ (2006) first reported that the E_2 high and A_1 (LO) peak positions change with increasing drain bias in the pinched OFF state relative to the zero bias state despite the negligible temperature rise associated with near zero dissipated power [12]. The authors attributed the change in Stokes peak positions to stress and strain induced by the inverse or converse piezoelectric effect but observed an order of magnitude disagreement between the values of stress and strain derived from micro-Raman measurements and those predicted by electrical device modeling. Sarua $et\ al.$ (2006) also suggested that the pinched OFF state with the same drain bias as the ON state should be used as the reference for temperature measurements based on the change in Stokes peak position rather than the zero bias state. Subsequent reports have confirmed that measuring the changes in Stokes peak position and/or linewidth with the pinched OFF state as a reference results in temperature values in good agreement with Stokes/anti-Stokes and thermomechanical modeling [7]-[9]. However, a clear, quantitative description of the electro-mechanical state of the GaN layer(s) in the pinched OFF state has remained elusive [13]-[14].

In this paper, we review the previous work on experimental characterization of IPE stress and strain in GaN HEMTs via micro-Raman spectroscopy in an effort to better understand the use of the pinched OFF state as a reference for temperature measurements. First, we describe the experimental technique and discuss popular methods for extracting the GaN temperature rise from changes in the Stokes peak positions. We perform electrical device modeling of a GaN HEMT and

uncoupled electro-mechanical modeling of the GaN buffer to clarify the mechanism of IPE stress and strain in the GaN buffer and to examine how mechanical boundary conditions affect the depth-averaged values of these quantities. Next, we review the relevant material properties used to relate changes in Stokes peak positions to stress and strain and suggest that uncertainty in the values of these material properties does not explain the discrepancy between the measured and predicted values of stress and strain. We analyze published experimental data on the changes in Stokes peak positions and show that extracted values of the stress and strain do not agree in sign and/or order of magnitude with predicted values from electrical and electro-mechanical modeling, depending upon which Raman peaks are considered in the analysis. In particular, we find that several hypotheses offered in the literature for these discrepancies, including (i) uncertainties in the material properties, (ii) non-classical piezoelectric coupling, and (iii) correlation between the peak electric field and depth-averaged stress, are not supported by our model and the published experimental data. Finally, we suggest that the electric field in the pinched OFF state could strongly affect the Stokes peak position apart from the IPE-induced strain and highlight several open questions in the field.

II. Experimental Technique

A. Micro-Raman Spectroscopy

Raman spectroscopy is one of the most common experimental techniques for identifying materials and characterizing their structure, quality, temperature and other properties by measuring the frequencies of their vibrational modes [15], particularly for III-nitride semiconductors [16]. In the Raman scattering process, an incident photon with wavelength λ_0 is scattered to a wavelength

λ by emitting (Stokes process) or absorbing (anti-Stokes process) a phonon. The relative change in wavenumber of a photon before and after a Raman scattering event

$$\omega = \frac{1}{\lambda_0} - \frac{1}{\lambda} \tag{1}$$

is directly proportional to the frequency of the phonon emitted or absorbed in the Raman scattering process and is thus a measure of the phonon frequency. Due to the fact that photons carry a significant amount of energy but little momentum and phonons have relatively low energies but large momenta, Raman scattering in semiconductors generates and absorbs only optical phonons near the center of the first Brillouin zone (Γ-point). Momentum conservation and crystal symmetry considerations place further constraints on the optical phonon modes that may be observed for a given scattering configuration, *i.e.*, the incoming and scattered photon directions relative to the crystallographic orientation, which lead to selection rules. In this work, we mainly discuss the Stokes process associated with optical phonon emission and use the terms "Stokes peak position," "Raman peak position," and "phonon frequency" interchangeably as they refer to quantities that are directly proportional to each other.

Micro-Raman spectroscopy specifically involves the focusing of the laser excitation to a micron size spot on the sample whose diameter and collection depth are limited by the diffraction of light. Notch or edge filters are needed to block the Rayleigh scattered light at the excitation wavelength λ_0, and the Raman scattered light is dispersed into a spectrum with a spectrometer or monochromator. A phonon mode generated by Raman scattering appears as a peak with a center position corresponding to the phonon frequency and a finite linewidth associated with the phonon lifetime and instrumental response, *i.e.*, the point spread function, of the spectrometer [17]. The precision with which a change in the Raman peak position can be measured depends on the optical

characteristics of the spectrometer (grating groove density, focal length, and slit width), pixel size of the detector, and features of the Raman peak (intensity, linewidth, and proximity to other peaks). The highest precision is achieved by fitting a Raman peak with a lineshape, such as a Lorentzian, Gaussian, or Voigt profile, to determine the center of the peak for each measurement [18]. Uncertainties in the change in Raman peak position as small as 0.01 cm^{-1} based on the random error of repeated measurements are possible with commercially-available micro-Raman systems, frequency-stabilized laser sources, and careful spectrometer calibration.

B. GaN High Electron Mobility Transistors

GaN-based transistors have attracted significant interest in recent years due to the material's wide bandgap, high critical electric field, and potential to develop a variety of heterostructures with epitaxial layers of alloys of other III-nitride semiconductors [19]. In particular, the AlGaN/GaN heterostructure results in a high density two-dimensional electron gas (2DEG) due to a difference in spontaneous and piezoelectric polarization between the two materials [20]. The unique combination of high electron concentration and mobility of the 2DEG and high critical electric field of AlGaN and GaN layers simultaneously allows for high operating voltages and current densities in the lateral HEMT structure. Thus, GaN HEMTs can operate at significantly higher power densities for radio-frequency (RF) and microwave power amplifier (PA) applications than other semiconductor devices, such as those based on gallium arsenide [1],[21]. GaN HEMTs also exhibit excellent performance at high switching frequencies and efficiency savings in power conversion applications because of their low on-resistances and high breakdown voltages [22].

Due to the challenges in growing bulk GaN substrates in large sizes and with low defect densities, GaN is typically grown on a foreign substrate, such as sapphire, silicon carbide (SiC), or silicon. For high performance GaN PAs with significant power dissipation, SiC is preferred as a substrate because of its high thermal conductivity (420 W/m-K) compared to silicon (150 W/m-K) and sapphire (35 W/m-K) [5]. Both GaN and SiC (4H-SiC and 6H-SiC) are wurtzite crystals belonging to the point group C_{6v} with a hexagonal Bravais lattice. In the epitaxy process, typically 1 to 2 μm of GaN is grown on the (0001) plane (c-plane) of SiC after AlN and/or AlGaN nucleation and stress management layers are deposited so that the [0001] direction or c-axis of GaN and SiC are aligned. A much thinner AlGaN barrier of 15 to 30 nm is grown on the top of the GaN buffer to form the heterojunction and 2DEG. Transistors are fabricated on AlGaN/GaN heterostructures by forming ohmic contacts for the source and drain and a Schottky or metal-insulator-semiconductor contact for the gate. Schematics of the wurtzite GaN unit cell, crystal structure, and basic HEMT structure are shown in Figure 1. The difference in lattice constants and coefficient of thermal expansion between the epitaxial layers results in residual stress/strain in the GaN buffer and AlGaN barrier when the wafer is cooled to room temperature. For other substrates, thicker GaN epilayers and/or more complex nucleation and stress management layers may be needed to provide the desired electrical properties of the buffer and prevent cracking [24].
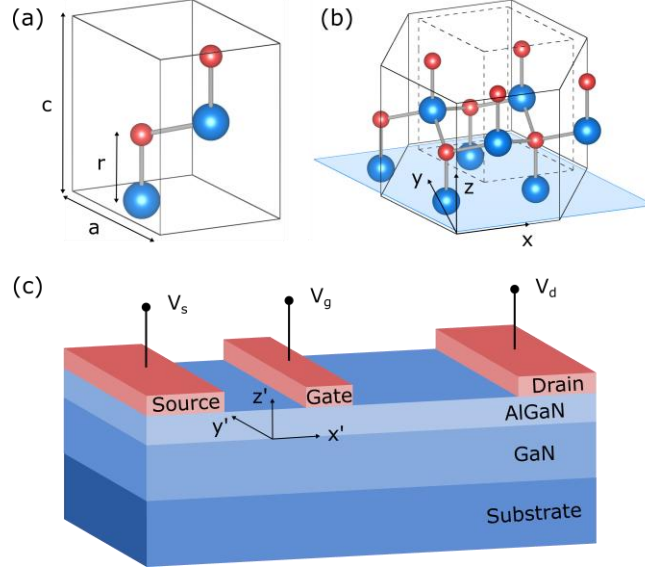
FIG. 1. (a) Wurtzite GaN unit cell, (b) crystal structure, and (c) basic GaN HEMT structure. Larger blue and smaller red spheres denote Ga and N ions, respectively. Crystal structures were drawn with the VESTA visualization software [23]. The drain and gate biases are referenced with respect to the source, i.e., $V_{ds} = V_d - V_s$ and $V_{gs} = V_g - V_s$.

The hexagonal lattice structure of wurtzite GaN depicted in Figure 1 (a) and (b) is described by two lattice parameters, a and c, and a third internal structural r parameter denoting the distance between the Ga and N atoms or bond length along the c-axis. In the Miller-Bravais index system ($hki\ell$) [25], the x-axis of the hexagonal crystal structure is chosen to be the [11-20] direction, and the z-axis set equal to the c-axis or [0001] direction [26]-[27]. In order to form a mutually orthogonal, right-handed coordinate system, the y-axis is then chosen to be the [-1100] direction. This crystallographic coordinate system is used to define the tensor components of the material properties of wurtzite GaN, which must be invariant under the symmetry operations of the point group C_{6v}. However, there is also the need to define a convenient coordinate system x',y',z' with respect to the features of a lateral GaN HEMT, such as the channel and gate contact. As mentioned previously, GaN epilayers grown on SiC substrates have the c-axis of the two materials aligned so it is natural to choose the z'-axis of the transistor to be the same as the z-axis of the crystal.

Following previous works [12], we chose the x'- and y'-axes to correspond to the directions perpendicular to and along the gate, respectively, as shown in Figure 1 (c). Depending on how a transistor is fabricated with respect to the crystallographic planes, there is the possibility of a difference in angle θ of rotation between the x- and x'-axes of the crystallographic and transistor coordinate systems, respectively. We address this issue and its implications in detail in Section II. C. and Appendix A, showing that it does not affect the interpretation of changes in micro-Raman spectra related to IPE-induced stress and strain.

Raman spectra from GaN HEMTs are typically measured in the $\bar{z}(\cdot\cdot)z$ backscattering configuration, in which the laser excitation is directed along the [000-1] direction of wurtzite GaN by a microscope objective and the Raman scattered light is collected by the same objective along the reverse path. Raman selection rules specify that only three of the nine possible optical phonon modes, assigned the labels E_2 high, E_2 low, and A_1 (LO) from group theory, are accessible in the $\bar{z}(\cdot\cdot)z$ backscattering scattering configuration in wurtzite GaN [28]. While the E_2 modes are observable with the polarization of the laser parallel, i.e., $\bar{z}(xx)z$ or $\bar{z}(yy)z$, and perpendicular, i.e., $\bar{z}(xy)z$ or $\bar{z}(yz)z$, to that of the collection optics, the A_1 (LO) mode is only observable in the parallel polarization configuration. Measurements of the E_2 high mode are most common due its high intensity for samples of good crystal quality. Characterization of the A_1 (LO) mode is also common although it is broader and less intense than the E_2 high mode. The E_2 low mode is rarely reported in the literature due to its low frequency (140 to 145 cm^{-1}), low intensity, and very narrow linewidth, making it difficult to measure except with high resolution spectrographs and optical filters with very sharp transitions near the laser wavelength. In most studies, microscope objectives of 50× to 100× magnification with numerical apertures (NA) of 0.5 to 0.6 result in a laser spot size of ≈1 to 1.3 µm [4],[9]. Objectives with higher NA values and smaller associated laser spot

sizes are widely available but difficult to use with on-wafer devices due to the need for a substantial working distance to accommodate electrical probes. The depth of field, also determined by the laser wavelength and NA and magnification of the objective, is often ≈1 to 3 µm, depending upon the confocal pinhole size if present [4],[29]. These considerations with respect to focusing of the laser and collection of scattered light by the objective mean that the Raman spectrum is collected from a volume extending throughout the depth of the GaN epitaxial layer(s) (1 to 2 µm) with a diameter of ≈1 µm. Thus, temperature, stress, and strain values extracted from micro-Raman spectroscopy represent area- and depth-averaged values of these quantities, which may vary significantly within the excitation/collection volume both laterally and across the GaN layer(s). A schematic of micro-Raman spectroscopy of GaN HEMTs is shown in Figure 2 with a sample spectrum of a GaN epilayer structure on 4H-SiC.
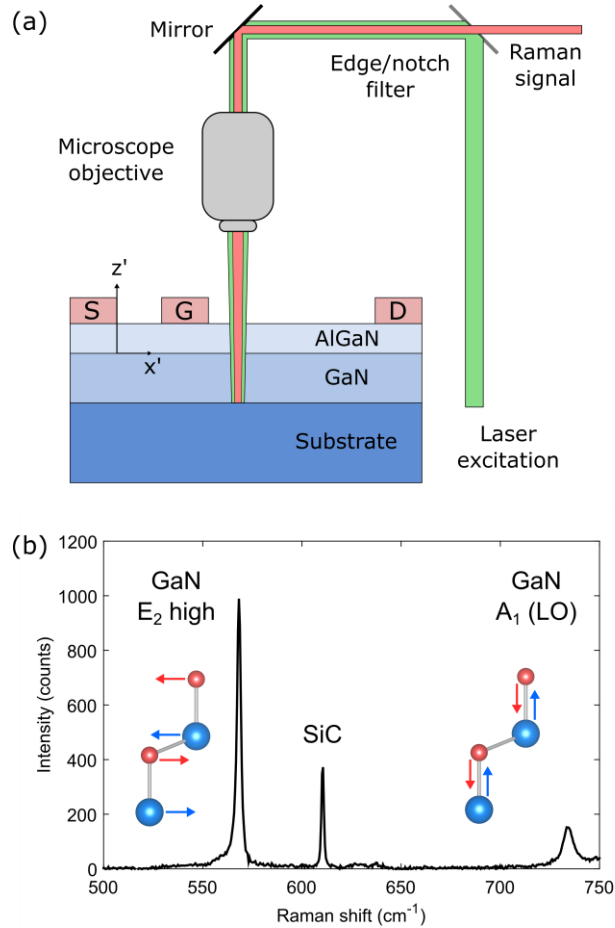
FIG. 2. (a) Schematic of micro-Raman spectroscopy technique on GaN HEMTs and (b) sample spectrum of a GaN on 4H-SiC substrate with 532 nm laser excitation with phonon modes depicted in the inset. The schematic in (a) is not drawn to scale.

C. Micro-Raman Thermometry in GaN HEMTs

Although commercially-available, high resolution spectrometers are capable of measuring Stokes peak position changes as small as 0.01 cm^{-1} by fitting a lineshape (typically a Voigt profile) to the Raman peaks of GaN, the accuracy with which temperature can be measured also depends on the accuracy of the relationship between temperature and peak position determined by calibration. Empirical relations for the dependence of the Stokes peak position on temperature have been proposed in the GaN literature, such as

$$\omega(T) = \omega_0 - \frac{A}{\exp(B\hbar\omega_0/k_B T) - 1} \tag{2}$$

where $\omega(T)$ is the Stokes line position, T is the absolute temperature, ω_0 is the Stokes line position at absolute zero temperature, and A and B are fitting constants determined by calibration [11],[30]. However, this relation is not rigorously derived from crystal lattice dynamics and does not provide a physical explanation for the reason GaN free standing and epitaxial films have different values of the parameters ω_0, A, and B. In contrast, a clear relationship between the optical phonon frequency and temperature has been derived from a quantum mechanical treatment of crystal lattice dynamics including anharmonic effects

$$\Delta\omega = \omega(T) - \omega(T_0) = \Delta\omega_{strain} + \Delta\omega_{decay} \tag{3}$$

where $\Delta\omega$ is the change in total change in phonon frequency due to a change in temperature from a reference state at temperature T_0 and $\Delta\omega_{strain}$ and $\Delta\omega_{decay}$ are the contributions from thermal expansion and phonon-phonon interactions, respectively [31]-[32]. While discussion of the exact expression for $\Delta\omega_{decay}$ is beyond the scope of this paper, Equation (3) is particularly useful in understanding the mechanisms responsible for phonon frequency shift with temperature. Thermal expansion results in strain, which changes the interatomic potential between atoms and force constants, and a change in temperature also affects the phonon-phonon scattering processes by changing the phonon occupation probability. Thus, Equation (3) applies to GaN epitaxial layers, free standing films, and bulk substrates. The phonon frequency shift due to thermal expansion $\Delta\omega_{strain}$ is different for each kind of GaN sample because the mechanical constraints on a sample determine the amount of thermal strain for a given temperature rise. In contrast, the phonon frequency shift associated with phonon-phonon interactions $\Delta\omega_{decay}$ should only depend on the

12

intrinsic properties of GaN and should be relatively sample-independent. It is immediately evident that any other crystal effect that induces strain, such as the IPE effect, could shift the phonon frequency in addition to thermal expansion. Although the $\Delta\omega_{decay}$ contribution to the phonon frequency shift varies nonlinearly with absolute temperature, it has been observed that the change in phonon frequency with temperature is approximately linear with temperature from 25 °C to 300 °C for both GaN epitaxial films on SiC substrates and bulk GaN samples [8]-[9].

Understanding the strain contribution to the phonon frequency shift $\Delta\omega_{strain}$ of the GaN buffer in a HEMT requires a detailed analysis of the piezoelectric and thermoelastic contributions to the strain for a given bias condition. When a GaN HEMT is biased in the ON state, $i.e.$, $V_{ds} = V_d - V_s > 0$ and $V_{gs} = V_g - V_s > V_{th}$, where V_d, V_s, and V_g are the voltages of the drain, source, and gate contacts, respectively, and V_{th} is the gate threshold voltage, there is an increase in temperature due to Joule heating and an electric field due relative to the zero bias state ($V_{ds} = 0$ and $V_{gs} = 0$). Because GaN is a piezoelectric, thermoelastic solid, the strain components at each point in the material are related to the stress, electric field, and temperature rise through the constitutive relation

$$\epsilon_i = s_{ij}\sigma_j + \alpha_i\Delta T + d_{ki}E_k \tag{4}$$

where ϵ_i is the strain vector written in contracted notation, σ_j is the stress vector, E_k is the electric field, s_{ij} is the elastic susceptibility tensor, α_i are the coefficients of thermal expansion, and d_{ki} are the piezoelectric moduli [25]. Under the continuum approximation, the strain tensor at each infinitesimal point x, y, z is defined by the gradient in the displacement vector $\vec{u}$

$$\epsilon_{ij} = \frac{1}{2}\left(\frac{\partial u_i}{\partial x_j} + \frac{\partial u_j}{\partial x_i}\right) \tag{5}$$

where $\vec{x} = x\hat{e}_1 + y\hat{e}_2 + z\hat{e}_3$ is the position vector [34]. From the perspective of the crystal lattice, the strain components are related to the change in lattice parameters

$$\epsilon_{xx} = \epsilon_{yy} = \frac{a - a_0}{a_0} \tag{6a}$$

$$\epsilon_{zz} = \frac{c - c_0}{c_0} \tag{6b}$$

where a_0 and c_0 are the unstrained lattice parameters if the normal strain is symmetric in the c-plane ($\epsilon_{xx} = \epsilon_{yy}$) [20]. If the strain is asymmetric in the c-plane ($\epsilon_{xx} \neq \epsilon_{yy}$) or contains non-zero shear strain components, the symmetry of the point group C_{6v} is broken and the wurtzite crystal can no longer be described by the lattice parameters a and c, which leads to expressions more complicated than Equations (6a) and (6b).

Linear potential deformation theory predicts that $\Delta\omega_{strain}$ for each phonon mode should be governed by the symmetry of the mode and that of the perturbation to the crystal potential V_{ij}' associated with the strain tensor ϵ_{ij}. For phonon modes belonging to the E₂ and A₁ representations in the point group C_{6v}, this relationship is given by the equations

$$\Delta\omega_{E_2} = a_{E_2}(\epsilon_{xx} + \epsilon_{yy}) + b_{E_2}\epsilon_{zz} \pm c_{E_2}\sqrt{(\epsilon_{xx} - \epsilon_{yy})^2 + 4\epsilon_{xy}^2} \tag{7a}$$

$$\Delta\omega_{A_1} = a_{A_1}(\epsilon_{xx} + \epsilon_{yy}) + b_{A_1}\epsilon_{zz} \tag{7b}$$

where a, b, and c are the strain phonon deformation potentials (PDPs) [33]. As noted in Section II. B., the crystallographic x,y,z coordinate system for which the strain components in Equations (7a) and (7b) are defined may differ from the transistor x',y',z' coordinate system by a rotation angle θ around the $z = z'$ axis. However, we show in Appendix A that the quantities $\epsilon_{xx} + \epsilon_{yy}$,

ϵ_{zz}, and $(\epsilon_{xx} - \epsilon_{yy})^2 + 4\epsilon_{xy}^2$ are invariant under rotation around the z-axis so that Equations (7a) and (7b) are equally valid in the transistor x',y',z' coordinate system. For the remainder of this paper, we drop the prime notation and use x,y,z to refer to the transistor coordinate system for convenience and without loss of generality.

As will be discussed in greater detail in Section III. A., the application of a positive drain bias results in a vertical electric field E_z along the c-axis in the GaN buffer, which is only related to the normal strains ϵ_{xx}, ϵ_{yy}, and ϵ_{zz} through the piezoelectric modulus tensor components $d_{31} = d_{32}$ and d_{33} [13],[25]. The electric field components in the c-plane E_x and E_y are coupled to the shear strain components ϵ_{xz} and ϵ_{yz}, respectively. However, there is no dependence of the E₂ high and A₁ (LO) frequencies on ϵ_{xz} and ϵ_{yz} in Equations (7a) and (7b), indicating that these components do not result in changes in the Raman peak positions observed in the backscattering configuration. The detailed form of the strain contribution to the E₂ high peak position in terms of the stress, temperature rise, and electric field components can be derived by inserting Equation (4) into Equation (7a)

$$\Delta\omega_{E_2} = \left[a_{E_2}(s_{11} + s_{12}) + b_{E_2}s_{13}\right](\sigma_{xx} + \sigma_{yy}) + \left[2a_{E_2}s_{13} + b_{E_2}s_{33}\right]\sigma_{zz}$$

$$\pm c_{E_2}|s_{11} - s_{12}|\sqrt{(\sigma_{xx} - \sigma_{yy})^2 + 4\sigma_{xy}^2} + \left[2a_{E_2}d_{31} + b_{E_2}d_{33}\right]E_z \qquad (8)$$

$$+ \left[2a_{E_2}\alpha_{xx} + b_{E_2}\alpha_{zz}\right]\Delta T$$

where we have used the identity $s_{66} = \frac{1}{2}(s_{11} - s_{12})$ for the point group C_{6v} [25]. The dependence of the A₁ (LO) peak position on these quantities is the same as Equation (8) with the exception of the third term associated with the asymmetric normal stress and shear stress in the xy-plane, which is omitted for the A₁ (LO) mode. The dependence of the E₂ high peak shift in Equation (8) contains

six unknown variables (σ_{xx}, σ_{yy}, σ_{zz}, σ_{xy}, E_z and ΔT) that could all simultaneously be affecting the E$_2$ high peak position under an arbitrary gate and drain bias applied to a GaN HEMT. These six unknown variables can be reduced to only three by evaluating the relative magnitudes of various terms in Equation (8).

Provided the GaN buffer behaves as a linear piezoelectric material, there should be negligible shear stress in the c-plane ($\sigma_{xy} \approx 0$) except for near the edges of the die [7]. In most experiments, the top surface of the GaN buffer is free to move because there is nothing to prevent it from expanding or contracting, leading to negligible stress along the c-axis ($\sigma_{zz} \approx 0$) [9]. Although the piezoelectric moduli d_{31} and d_{32} are equal, the normal strain and stress components in the c-plane are also determined by the spatial variation of the vertical electric field $E_z(x, y)$ and the mechanical boundary conditions imposed on the GaN buffer. Because of the inherent asymmetry of the lateral HEMT structure, the E_z electric field component varies significantly in the x-direction (along the channel) but is almost constant in the y-direction (parallel to the gate). Thus, one would expect that the strain and stress components in these two directions should not be equal ($\epsilon_{xx} \neq \epsilon_{yy}$ and $\sigma_{xx} \neq \sigma_{yy}$). According to Equation (8), asymmetry of the normal stress components in the c-plane would result in a splitting of the Raman peak position of the E$_2$ high mode between Raman spectra acquired in the parallel and cross-polarized configurations [27]. Previous measurements of GaN HEMTs biased in the pinched OFF state have reported that this splitting of the E$_2$ high mode is not detectable within experimental uncertainty [13]. This suggests that the asymmetry in the in-plane strain $\epsilon_{xx} - \epsilon_{yy}$ and in-plane stress $\sigma_{xx} - \sigma_{yy}$ is small compared to the values of the strain and stress components themselves. The assumption of symmetric IPE-induced strain and stress in the c-plane ($\epsilon_{xx} \approx \epsilon_{yy}$ and $\sigma_{xx} \approx \sigma_{yy}$) is then a good

approximation that allows one to further simplify Equation (8). Our 3D electro-mechanical model of the GaN buffer discussed in Section III. B. also suggests that the stress is approximately biaxial.

Taking of all of these simplifications into account, the change in Stokes peak position of the E_2 high and A_1 (LO) modes between the ON state and the zero bias state can be expressed as

$$\Delta\omega = \omega_{ON} - \omega_0 = K^{II}\sigma_{xx} + A\Delta T + BE_z \tag{9}$$

where ω_{ON} and ω_0 are the Stokes line positions of the ON state and zero bias state, respectively, K^{II} is the biaxial stress coefficient, A is the linear temperature coefficient, and B is the electric field coefficient. One should note that the values of stress, temperature difference, and electric field in Equation (9) are the differences in these quantities between the ON state and zero bias state, not absolute values of these quantities. In addition, the derivation of Equation (9) does not assume that the strains in the c-plane ϵ_{xx} and ϵ_{yy} are zero. The biaxial stress appearing in Equation (9) for an ON state bias is a combination of the biaxial stresses due to the IPE and thermoelastic effects. The biaxial stress coefficient K^{II} and IPE-related electric field coefficient B under these assumptions are given by

$$K_n^{II} = 2a_n(s_{11} + s_{12}) + 2b_n s_{13} \tag{10a}$$
$$B_n = 2a_n d_{13} + b_n d_{33} \tag{10b}$$

which have different values for the E_2 high and A_1 (LO) modes due to different values of the strain PDPs. The first term involving the strain PDP a is related to the in-plane strain components while the second term with b is related to the out-of-plane strain component.

If change in the Stokes peak position of only one phonon mode, such as the E_2 high mode, is measured from the zero bias state to the ON state, the temperature rise cannot be properly decoupled from the stress and electric field. Simultaneous measurement of two phonon modes,

usually the E_2 high and A_1 (LO), still cannot successfully isolate the temperature rise because there are two equations of the form of Equation (9) and three unknowns (σ_{xx}, ΔT, and E_z). Sarua *et al.* (2006) was the first to suggest that the pinched OFF state ($V_{ds} > 0$ and $V_{gs} < V_{th}$) at the same drain bias as the ON state should be used as the reference for temperature measurements rather than the zero bias state [12]. In the pinched OFF state, there is negligible current in the HEMT channel and negligible power dissipation, resulting in near zero temperature rise and thermoelastic stress. A schematic of the proposed measurement in the context of the drain current-drain voltage output characteristics (I_d-V_{ds}) is shown in Figure 3.
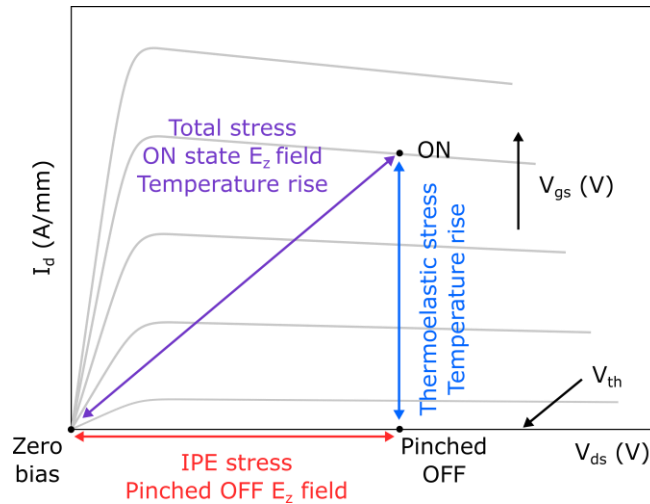

FIG. 3. Schematic representation of the contributions of stress, temperature rise, and electric field to Stokes peak position between different HEMT bias points in the drain current-drain voltage (I_d-V_{ds}) output characteristics. The gate threshold voltage V_{th} is the gate bias below which there is negligible drain current ($\lesssim$1 mA/mm).

The hypothesis that the difference in Stokes peak positions between the pinched OFF state and the zero bias state accounts for the IPE-induced stress and vertical electric field can only be true if the electric field in the pinched OFF state and the ON state is the same. In their seminal paper on this topic, Sarua *et al.* (2006) performed electrical device modeling and found this to be

approximately true [12]. Then, the contributions of the IPE effect and temperature rise can be written in terms of the difference in Raman peak positions between the ON state and the pinched OFF state $\Delta\omega_{ON/OFF}$ and the pinched OFF state and the zero bias state $\Delta\omega_{OFF/0}$

$$\Delta\omega_{ON/OFF} = \omega_{ON} - \omega_{OFF} = K^{II}\sigma_{xx}^{TE} + A\Delta T \qquad (11a)$$

$$\Delta\omega_{OFF/0} = \omega_{OFF} - \omega_0 = K^{II}\sigma_{xx}^{IPE} + BE_z \qquad (11b)$$

where σ_{xx}^{IPE} and σ_{xx}^{TE} are the stresses due to the IPE and thermoelastic effects, respectively. A more rigorous justification of Equations (11a) and (11b) and the conditions for which they apply are provided in Appendix B. Since the introduction of the pinched OFF state as the proper reference for micro-Raman thermography, temperature measurements of the ON state based on the Stokes peak position and linewidth have shown good agreement with Stokes/anti-Stokes measurements and thermal models [7]-[9]. Thus, it is widely accepted in the GaN electronics community that using the pinched OFF state properly accounts for the stress and/or strain induced by the IPE effect.

D. IPE Stress and Strain Measurement

Despite the importance of accounting for the contribution of the electric field and the IPE-induced stress and popularity of using the pinched OFF state as the reference, relatively few papers have attempted to quantify the electric field magnitude and IPE stress/strain in the pinched OFF state. Assuming the average vertical electric field across the GaN buffer to be the same in the ON state and pinched OFF state at the same drain bias, the change in Stokes peak position between the pinched OFF and the zero bias states should provide a self-consistent measurement of the induced IPE stress and vertical electric field according to Equation (11b). However, because Equation (11b) involves the two unknowns of stress σ_{xx}^{IPE} and vertical electric field E_z, measurement of the changes in the Stokes peak position of two modes are needed in principle. The most common

experimental method described in the literature to characterize the induced stress and strain is to (i) measure the Raman spectrum of a GaN HEMT in the zero bias state at a particular location and (ii) measure the same location in the pinched OFF state [8],[12]-[14]. Under the assumption of negligible shear strain and symmetric normal strains in the c-plane described in Section II. C., the changes in the frequency of the E_2 high and A_1 (LO) modes may be related to the normal strain components by the set of two equations

$$\begin{bmatrix} \Delta\omega_{E_2} \\ \Delta\omega_{A_1} \end{bmatrix} = \begin{bmatrix} 2a_{E_2} & b_{E_2} \\ 2a_{A_1} & b_{A_1} \end{bmatrix} \begin{bmatrix} \epsilon_{xx} \\ \epsilon_{zz} \end{bmatrix} \tag{12}$$

where $\Delta\omega_{E_2}$ and $\Delta\omega_{A_1}$ represent the change in frequency of the E_2 high and A_1 (LO) modes between the pinched OFF state and zero bias state, respectively. Using the simplified form of the constitutive relation in Equation (4) and assuming $\sigma_{xx} = \sigma_{yy}$, the normal strain components can also be related to the in-plane stress and vertical electric field through the set of two equations

$$\begin{bmatrix} \epsilon_{xx} \\ \epsilon_{zz} \end{bmatrix} = \begin{bmatrix} s_{11} + s_{12} & d_{31} \\ 2s_{13} & d_{33} \end{bmatrix} \begin{bmatrix} \sigma_{xx} \\ E_z \end{bmatrix} \tag{13}$$

Equations (12) and (13) thus provide a self-consistent experimental method for characterizing the induced strain, stress, and vertical electric field when a GaN HEMT is pinched off based on measurements of changes in E_2 high and A_1 (LO) frequency with the drain bias.

Due to the fact that lateral HEMTs for high frequency applications have a limited breakdown voltage associated with their relatively small gate-drain spacing of 2 to 4 µm, Sarua *et al.* (2010) introduced an alternate structure for characterizing IPE stress and strain [13]. The authors utilized two ohmic contacts on a standard AlGaN/GaN heterostructure that were electrically isolated by etching through the 2DEG at the AlGaN/GaN interface as shown in Figure 5 in Ref. [13]. Voltage differences between the two pads were applied up to 150 V and the changes

in E_2 high and A_1 (LO) peak positions monitored near the edge of the positively biased pad (termed the drain) where the peak vertical electric field was expected [13]. When measured on the same epitaxial structure as lateral HEMTs, this pair of mesa-isolated contact pads permits higher induced stress and strains for more comprehensive characterization.

III. Modeling

Due to the complexity of the electric field distribution in a GaN HEMT and tensor nature of the stress and strain fields, electrical and electro-mechanical device modeling can provide helpful insight to guide the interpretation of experimental data from micro-Raman spectroscopy. Because the work by Sarua *et al.* (2006) is essentially the basis for using the pinched OFF state as the reference in micro-Raman thermometry, it is critically important to understand the key physics of the vertical electric field in the GaN buffer and the strain and stress fields it induces. Toward this goal, we discuss electrical modeling with the semiconductor device modeling software Silvaco ATLAS/BLAZE but from a different perspective than that of Sarua *et al.* (2006). We complement this device model with an uncoupled electro-mechanical model in COMSOL Multiphysics to investigate the nature of the IPE-induced strain and stress in the GaN buffer. In contrast to previous works [12]-[14], we have predicted the stress and strain distributions from the electro-mechanical model and the appropriate boundary conditions on the surfaces of the GaN buffer in order to understand the impact of these boundary conditions on the depth-averaged values of stress and strain that are correlated to Raman peak shifts. Although we modeled a specific GaN HEMT with the same dimensions as that of Sarua *et al.* (2006) [12] in order to compare our model with their experimental data, the conclusions regarding the electric field, stress, and strain distributions in the channel are widely applicable to a variety of devices with different layouts.

A. Electrical Device Modeling

Because of the difference in bandgap, electron affinity, and doping level of the materials present in an AlGaN/GaN HEMT, there is essentially always a built-in potential across the GaN buffer and vertical electric field in the zero bias state. When a positive drain bias ($V_{ds} > 0$) is applied in the OFF state ($V_{gs} < V_{th}$), the drain bias raises the electric potential at the top of the GaN buffer with respect to the bottom of the buffer. This difference in potential results in an additional vertical electric field primarily in the gate-drain access region and under the drain contact along the c-axis [12]. By convention, the positive z-axis for the wurtzite system is chosen to coincide with the c-axis pointing from the substrate to the AlGaN barrier for Ga-face grown GaN epilayers [20]. Thus, the vertical electric field in the gate-drain access region induced by a positive drain bias must have a negative sign, *i.e.*, point along the negative z-axis, to be consistent with the sign convention chosen for the piezoelectric constants. This point regarding the sign of the vertical electric field, although basic, is crucial to our understanding of the IPE-induced strain and stress. It was not explicitly stated in the original paper by Sarua *et al.* (2006) but later noted by Sarua *et al.* (2010) and may be a continued source of confusion regarding the expected sign of the stress and strain components. In this work, we focus our discussion on the vertical electric field component E_z rather than the lateral components E_x and E_y because the changes in Stokes peak positions for the E2 high and A1 (LO) modes are not coupled to the lateral electric field components, as was discussed in Section II. B.

In order to model the electric field distribution in the GaN-on-SiC HEMT structure reported by Sarua *et al.* (2006), we developed an electrical device model with the Silvaco ATLAS/BLAZE software similar to the authors [12]. The thicknesses of the Al$_{0.25}$Ga$_{0.75}$N barrier and GaN buffer

were 30 nm and 1.2 µm, respectively. A 100 nm thick AlN nucleation layer was included between the GaN buffer and 4H-SiC substrate as is typical in GaN-on-SiC epitaxy. The gate length was 0.8 µm and the gate-drain and gate-source distances were 3.2 µm and 1.2 µm, respectively, based on Figure 2(a) in Ref. [12]. A positive sheet charge with a nominal concentration 10^{13} cm^{-2} was introduced at the AlGaN/GaN interface to account for polarization effects, resulting in a simulated threshold voltage of $V_{th} \approx$ -4.2 V. The unpowered OFF state and pinched OFF state were simulated in this model at a gate bias of V_{gs} = -6 V for which the drain current is less than 1 µA/mm. Deep acceptor-type traps with a density of 3.0×10^{16} cm^{-3} were introduced into the GaN buffer to account for impurities that result in a space charge region in the buffer when the drain contact is positively biased. For simplicity, self-heating effects were not included in the model as the impact of channel temperature on device characteristics was not the focus of this study.

While previous works have provided plots of the electric field distribution in the GaN buffer, we believe that the electric potential distribution can provide more intuitive physical insight in this situation. Assuming the collection volume in micro-Raman spectroscopy samples all of the Raman scattered light emitted from a ≈1 µm diameter spot through the thickness of the GaN buffer, the extracted values of strain, stress, and electric field according to Equations (7a) to (9) represent the depth-averaged values of these quantities. Although the constitutive relation expressed in Equation (4) applies only to an infinitesimal point x,y,z in the GaN buffer, an identical equation for the depth-averaged quantities can be derived by applying the average value theorem to each term

$$\bar{\epsilon}_i = s_{ij}\bar{\sigma}_j + \alpha_i \Delta \bar{T} + d_{ki}\bar{E}_k \tag{14}$$

where the quantity with the overbar $\bar{u} = \frac{1}{L}\int_{-L}^{0} u(z)dz$ is the value averaged through the depth of the GaN buffer. This depth-averaged constitutive relation does assume, however, that the elastic susceptibility, coefficients of thermal expansion, and piezoelectric moduli are constant over the volume of interest. Noting that by definition the electric field is minus the gradient of the electric potential $\vec{E} = -\nabla\varphi$, the average z-component of the electric field is given by

$$\bar{E}_z = \frac{1}{L}\int_{-L}^{0} E_z(z)dz = \frac{1}{L}\int_{-L}^{0} -\frac{\partial\varphi}{\partial z}dz = -\frac{\varphi(0) - \varphi(-L)}{L} \tag{15}$$

where L is the thickness of the buffer, which is exactly the difference in electrostatic potential across the GaN buffer divided by the thickness of the buffer with the proper sign. Therefore, it is easier to see by inspection how the average vertical electric field changes with the gate and drain bias from contour plots of the electric potential rather than the vertical component of the electric field. Finally, we note that the default sign convention assigned to the vertical axis in the Silvaco ATLAS/BLAZE software is opposite of the convention for the wurtzite system. Silvaco ATLAS/BLAZE chooses the positive z-axis to point from the top to the bottom of the GaN buffer when a GaN HEMT structure is modeled as in Sarua *et al.* (2006) [12] and this work. The electric potential for the GaN-on-SiC HEMT modeled in this work is shown in Figure 4 under four bias conditions: (a) the zero bias state $V_{ds} = 0$ V and $V_{gs} = 0$ V, (b) the unpowered OFF state $V_{ds} = 0$ V and $V_{gs} = $ -6 V, (c) the ON state with $V_{ds} = 20$ V and $V_{gs} = 0$ V, and (d) the pinched OFF state with $V_{ds} = 20$ V and $V_{gs} = $ -6 V.
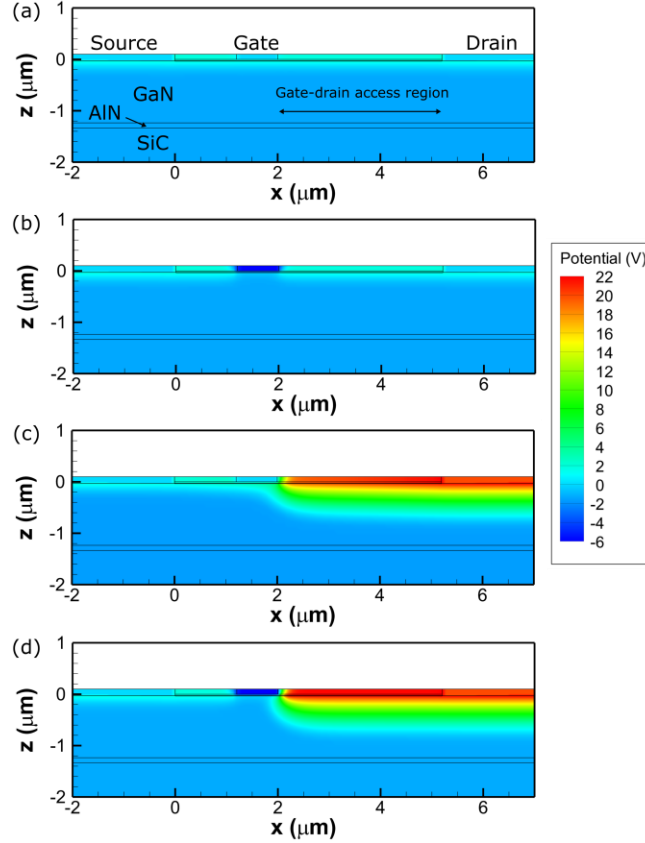
FIG. 4. Electric potential distribution for the GaN HEMT structure reported in Ref. [12] for (a) the zero bias state $V_{ds} = 0$ V and $V_{gs} = 0$ V , (b) the unpowered OFF state $V_{ds} = 0$ V and $V_{gs} = -6$ V, (c) the ON state with $V_{ds} = 20$ V and $V_{gs} = 0$ V, and (d) the pinched OFF state with $V_{ds} = 20$ V and $V_{gs} = -6$ V.

When the device is in the zero bias state (all contacts grounded), there is a built-in potential of 3.4 V across the 1.2 µm thick GaN buffer due to the band alignment in equilibrium as shown in Figure 4(a). As a negative bias is applied to the gate while the drain and source are grounded, the 2DEG underneath the gate is depleted while the electric potential of the bulk of the buffer remains almost unchanged, which can be seen in the small difference between Figure 4(a) and (b). The application of a positive drain bias raises the electric potential at the top of the GaN buffer, inducing a potential difference across the buffer in most of the gate-drain access region and under the drain contact as seen in Figure 4(c) and (d). Meanwhile, the potential difference across the buffer in the source-gate access region and under the source contacts is virtually unchanged

25

because the source contact has electrostatic control over this region of the device. There is only a minor difference in the potential difference across the GaN buffer between the ON state and the pinched OFF state at $V_{ds} = 20$ V. The surface potential of the buffer in the ON state is slightly lower than in the pinched OFF state because of the ohmic drop across the resistance gate-drain access region when there is significant current in the ON state. As first proposed by Sarua *et al.* (2006) [12], this behavior suggests that the pinched OFF state at a certain drain bias provides an accurate estimate of the IPE stress and strain present in the ON state at the same drain bias because the drain bias primarily determines the vertical electric field in the gate-drain access region and under the drain contact.

B. Electro-mechanical Modeling

As discussed in the previous section, the application of a positive drain bias in the pinched OFF state induces a difference in electric potential across the GaN buffer and vertical electric field predominately in the gate-drain access region of the channel and underneath the drain contact. This vertical electric field induces a combination of mechanical stress and strain according to the constitutive relation in Equation (4) such that the mechanical stress satisfies the static equilibrium condition

$$\nabla \cdot \overleftrightarrow{\sigma} = 0 \tag{16}$$

and any conditions on the stress or displacement components at the boundaries. Hence, the vertical electric field may be considered as the input needed to solve Equations (4) and (16) simultaneously for the stress and strain at each point in the HEMT structure. If the material properties and electrical behavior of a GaN HEMT are not significantly affected by the induced stress and strain, an uncoupled electro-mechanical model that calculates the stress and strain distributions from the

electric potential distribution provides a good approximation to the fully-coupled electro-mechanical problem. While a fully-coupled electro-mechanical model of a GaN HEMT could be needed to assess the impact of the very high electric field (~1 MV/cm) near the gate contact on stress in the AlGaN buffer [35], the much smaller electric field, stress, and strain magnitudes in the GaN buffer can be predicted accurately with an uncoupled model.

Due to the complexity in solving this 3D electro-mechanical problem for the strain and stress distributions, several further simplifications have been made in the literature for GaN HEMTs. One of these simplifications is the 2D plane strain approximation [34]-[35], which assumes that the normal strain along the gate ϵ_{yy} and the shear strain components ϵ_{xy} and ϵ_{yz} are zero because the gate width of a lateral GaN HEMT is typically much longer than the channel length, and the vertical electric field distribution $E_z(x, z)$ is approximately the same for each plane parallel to the xz-plane within the active HEMT area. The GaN buffer is prevented from deforming in the y-direction because of the clamping by the buffer outside the active area (in which the vertical electric field is zero) and by the substrate underneath the buffer in the active area. As a result of this mechanical constraint in the y-direction, there must be a corresponding normal stress along the gate $\sigma_{yy} \neq 0$. Another assumption, which has been commonly used in interpreting changes in micro-Raman spectra due to IPE-induces strain and stress, is that the GaN buffer is rigidly clamped in the c-plane by the substrate [12]-[14]. This implies that the bottom surface of the buffer has zero displacement under a vertical electric field E_z of any magnitude. Due to the high stiffness of wurtzite GaN, it also suggests that the normal strain components in the c-plane through the thickness of the buffer are approximately zero ($\epsilon_{xx} \approx 0$ and $\epsilon_{yy} \approx 0$).

In this work, we developed a 3D uncoupled electro-mechanical model of the GaN buffer (1.2 µm), AlN nucleation layer (100 nm), and 4H-SiC substrate (100 µm) using the finite element

software COMSOL Multiphysics to calculate the stress and strain distributions due to the IPE effect [36]. In the 3D model, we included the nucleation layer and substrate to evaluate the impact of the finite stiffness of these layers on the in-plane strain components. We also calculated the stress and strain distributions for 2D models under the plane strain approximation in the xz-plane with and without the AlN nucleation layer and SiC substrate to evaluate the impact of these approximations. In this section and throughout the remainder of the paper, we use the term "in-plane" to refer to the stress and strain components in the c-plane and "out-of-plane" to refer to the components along the c-axis, which coincides with the z-axis. Strictly speaking, the change in Stokes peak position between the zero bias state and the ON state given by Equation (9) is associated with a difference in vertical electric field between the two states rather than the absolute value of the vertical electric field in the ON state. Hence, one should subtract the potential distribution shown in Figure 4(a) from that shown in Figure 4(c) to obtain the appropriate depth-averaged value of E_z in Equation (9). Because the electric potential distribution is almost the same in the pinched OFF state and the ON state, one could choose either the zero bias state or the unpowered OFF state ($V_{gs} < V_{th}$) to subtract from the pinched OFF state. For consistency, we have chosen to subtract the potential distribution in the unpowered OFF state at the same gate bias as the pinched OFF state from that in the pinched OFF state for the electro-mechanical model.

The resulting electric potential distribution was imported from the Silvaco ATLAS/BLAZE simulation for the pinched OFF state at $V_{ds} = 20$ V and $V_{gs} = -6$ V with the unpowered OFF state at $V_{ds} = 0$ V and $V_{gs} = -6$ V subtracted. Values of the elastic and piezoelectric constants for GaN were taken from measurements on ammonothermal bulk GaN crystals [37]. Elastic and piezoelectric constants for AlN and SiC were taken from Refs. [38]-[41]. The top surface of the GaN buffer was set to a free surface on which all of the stress components are zero

28

because there are no forces to prevent the top of the GaN buffer from moving. The bottom of the

SiC substrate was constrained to zero displacement and the left and right boundaries of all layers

were assigned a symmetry condition on the displacement so that they could only deform along the

z-axis. In the 2D electro-mechanical model without the nucleation layer and substrate, the bottom

of the GaN buffer was constrained to zero displacement. Contour plots of the resulting vertical

electric field, strain, and stress distributions from the 3D electro-mechanical model in the xz-plane
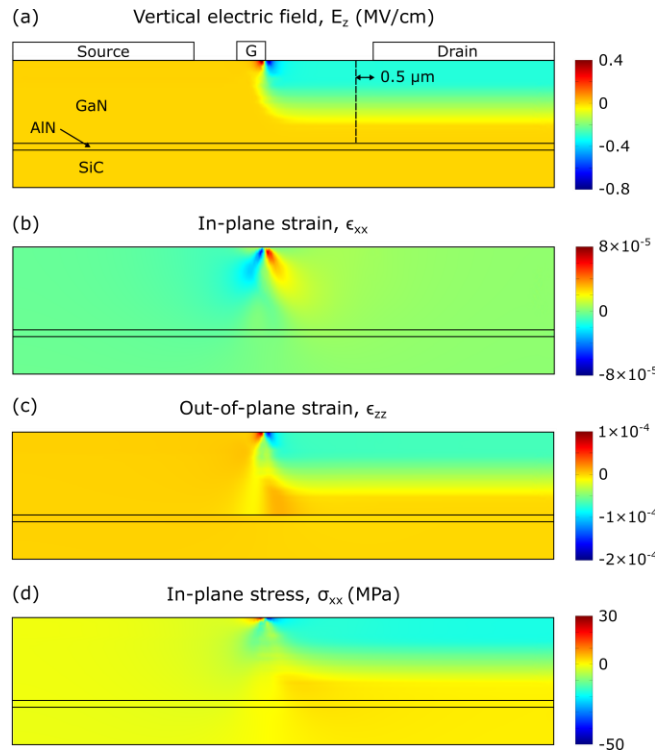
at the center of the gate are shown in Figure 5.

FIG. 5. Results extracted from electro-mechanical model for GaN buffer in the pinched OFF state at $V_{ds} = 20$ V and $V_{gs} = -6$ V in the xz-plane at the center of the gate (a) vertical electric field and (b) in plane strain, ϵ_{xx} (c) out-of-plane strain, ϵ_{zz}, and (d) in-plane stress, σ_{xx}. The dashed line in (a) indicates a line 0.5 µm to the left of the edge of the drain over which the depth-averages in the z-direction were computed.

The vertical electric field distribution in Figure 5(a) confirms that the vertical electric field

is negative throughout the GaN buffer except for a narrow region directly under the gate contact.

In particular, the vertical E_z component attains a peak value of -0.77 MV/cm at the edge of the gate on the drain side and is fairly uniform in the gate-drain access region and under the drain contact in the x-direction. In the z-direction, the magnitude of the E_z component decreases approximately linearly with z from the top to the bottom of the GaN buffer due to formation of a space charge region associated with filled acceptor-type traps. At a location 0.5 µm to the left of the drain contact, the E_z component attains a depth-averaged value of -0.165 MV/cm, which is equal to the drain bias divided by the thickness of the GaN buffer. Although the in-plane strain ϵ_{xx} attains both negative and positive values of ~10^{-4} near the gate, it has a small depth-averaged positive value of 5.46×10^{-6} along the indicated cutline in the gate-drain access region in Figure 5(a). As shown in Figure 5(c), the out-of-plane strain ϵ_{zz} closely resembles the E_z distribution with negative values that vary linearly from the top to the bottom of the GaN buffer. The depth-averaged value in the gate-drain access region is -3.72×10^{-5}, which is an order of magnitude larger than that of the in-plane strain with the opposite sign. Finally, we found that the in-plane stress σ_{xx} is compressive in the gate-drain access region with an average value of -8.30 MPa.

The quantitative values of these strain and stress components are affected by the approximations of 2D plane strain in the xz-plane ($\epsilon_{yy} = 0$) and rigid clamping of the GaN buffer by the substrate. In Table I, we list values of the depth-averaged normal strain and stress components and the vertical electric field along the cutline 0.5 µm to the left of the drain contact from our electro-mechanical models with and without these assumptions.

TABLE I. Depth-averaged values of the strain, stress, and electric field components along the line 0.5 µm to the left of the drain contact calculated from the electro-mechanical model under different approximations.

Quantity	2D plane strain without substrate	2D plane strain with substrate	3D with substrate
ϵ_{xx}	2.09×10^{-6}	6.46×10^{-6}	5.46×10^{-6}
ϵ_{yy}	0	0	7.32×10^{-7}
ϵ_{zz}	-3.61×10^{-5}	-3.72×10^{-5}	-3.72×10^{-5}
ϵ_{xy}	0	0	-6.41×10^{-11}
σ_{xx} (MPa)	-9.53	-8.03	-8.30
σ_{yy} (MPa)	-10.0	-9.53	-9.40
σ_{zz} (MPa)	0.065	0.046	0.019
E_z (MV/cm)	-0.165	-0.165	-0.165

As shown in Table I, there is a tensile strain along the gate $\epsilon_{yy} = 7.32 \times 10^{-7}$ in the full 3D model because the substrate cannot perfectly clamp the buffer from deforming along the y-direction. Since the strain components perpendicular to and along the gate are related through a strain compatibility relation [34]

$$\frac{\partial^2 \epsilon_{xx}}{\partial y^2} + \frac{\partial^2 \epsilon_{yy}}{\partial x^2} = \frac{\partial^2 \epsilon_{xy}}{\partial x \partial y} \qquad (17)$$

the presence of non-zero ϵ_{yy} in the full 3D model also slightly changes the value of ϵ_{xx} compared to the 2D models under the plane strain approximation. Rigid clamping of the bottom surface of the GaN buffer also results in lower values of the normal strain components and higher values of the normal stress components compared to the models with the nucleation layer and substrate included. In all cases, the out-of-plane strain ϵ_{zz} is an order of magnitude larger than ϵ_{xx} and two orders of magnitude larger than ϵ_{yy}. From Table I, one can see that there is a definite asymmetry in the in-plane strain $\epsilon_{xx} \neq \epsilon_{yy}$ and in-plane stress $\sigma_{xx} \neq \sigma_{yy}$ in all cases but that $|\sigma_{xx} - \sigma_{yy}| \ll |\sigma_{xx} + \sigma_{yy}|$, both of which appear in Equation (9). Based upon these values obtained from electro-

31

mechanical modeling and past experimental observations that parallel and cross-polarized Raman scattering does not result in a splitting of the E_2 high mode [13], we believe that the in-plane stress is approximately symmetric (biaxial) and that Equations (11a) to (13) are valid.

Although the quantitative values of stress and strain obtained from the 3D electro-mechanical model is specific to the device described in Ref. [12], it does provide general insights into the electro-mechanical state of the buffer in GaN HEMTs in the pinched OFF state, which should guide interpretation of the experimental data from micro-Raman spectroscopy experiments. The mechanical constraint at the bottom of the GaN buffer associated with clamping by the substrate causes the depth-averaged in-plane strain to be one order of magnitude lower than the out-of-plane strain, i.e., $|\bar{\epsilon}_{xx}| \ll |\bar{\epsilon}_{zz}|$. The free deformation of the top surface results in negligible average out-of-plane stress ($\bar{\sigma}_{zz} = 0.019$ MPa) through the depth of the GaN buffer compared to the in-plane stress. This finding contradicts the hypothesis by Beechem *et al.* (2008) [8] that a significant stress along the c-axis is induced in the pinched OFF state, which the authors supposed by observing that the E_2 high linewidth changes when the device is pinched OFF but remains constant under an applied uniaxial stress in the c-plane. Upon further investigation, it was found that directly applying a mechanical stress along the c-axis slightly changed the E_2 high linewidth but with a much smaller magnitude than in the pinched OFF state [42], which supports our finding from the electro-mechanical model that $|\bar{\sigma}_{zz}| \ll |\bar{\sigma}_{xx}|$. Considering the constitutive relation for the out-of-plane stress and setting its value equal to zero while neglecting the in-plane strain ($\epsilon_{xx} \approx \epsilon_{yy} \approx 0$)

$$\sigma_{zz} = 2C_{13}\epsilon_{xx} + C_{33}\epsilon_{zz} - e_{33}E_z \approx 0 \tag{18}$$

we obtain a simplified relation between the out-of-plane strain and the vertical electric field

$$\epsilon_{zz} \approx \frac{e_{33}}{C_{33}} E_z \qquad (19)$$

Since both constants e_{33} and C_{33} are positive, the out-of-plane strain ϵ_{zz} should have the same sign as E_z, which is negative in the gate-drain access region in the pinched OFF state with a positive drain bias. Using similar relations for the in-plane stress components σ_{xx} and σ_{yy}, one can show that the stress state is expected to be compressive in the c-plane and approximately biaxial with $\sigma_{xx} \approx \sigma_{yy}$, which we confirmed with the electro-mechanical model ($\bar{\sigma}_{yy}$ = -9.40 MPa).

It is important to note that, based on the constitutive relations expressed averaged over a certain volume as in Equation (12) and confirmed by the electro-mechanical model, the average values of stress, strain, and electric field are related to each other by Equation (14). This fact is actually independent of the thickness of the GaN buffer and the mechanical boundary conditions needed to solve Equation (16). Although it has been previously suggested that the average stress and/or strain measured by micro-Raman spectroscopy could be related to the peak electric field obtained from electrical device modeling [14], this would violate Equation (14) and the electro-mechanical model presented in this work. If measured values of the stress and strain components from micro-Raman spectroscopy are much higher than those predicted by the average vertical electric field (approximately the drain bias divided by the buffer thickness), it is not physical to assume that they could be related to the much higher peak electric field. The only assumptions underpinning Equation (14) and this conclusion are that the GaN buffer behaves as a linear elastic, piezoelectric solid under the continuum approximation, which is widely assumed in both modeling and experimental studies in the literature [9],[35],[43].

IV. Material Properties

Because micro-Raman spectroscopy measures only the shift in phonon frequencies in the GaN buffer induced by a vertical electric field in the pinched OFF state, the material properties relating phonon frequency shifts to electric field must be accurately known. In particular, this involves the phonon deformation potentials, which relate the phonon frequency shifts to strain components according to Equations (7a) and (7b), and the elastic and piezoelectric constants, which relate stress, strain, and electric field components according to Equation (4). Since inaccuracies in the measured and/or calculated values of these properties have been suggested as a source of discrepancies between the observed and expected values of the stress and strain components in the pinched OFF state [12], we have taken the opportunity here to review and tabulate values of these properties from the literature. In anticipation of the analysis presented in Section V, we believe that the relatively small variation in these properties reported by different references particularly over the last five years on GaN samples with improving crystal quality are not a likely source of these discrepancies.

A. Elastic and Piezoelectric Constants

Both modeling and experimental characterization of the strain and stress induced in a GaN HEMT by the inverse piezoelectric effect require accurate values of the elastic stiffness C_{ij} or susceptibility s_{ij} constants and the piezoelectric strain d_{ij} or stress moduli e_{ij}. Depending upon whether the stress or strain components are known by measurement or simple approximations, alternate forms of the constitutive relations are useful. These constitutive relations, which are equivalent to Equation (4) for zero temperature change, can be written in two different forms by isolating the strain or stress components

$$\epsilon_i = s_{ij}\sigma_j + d_{ki}E_k \tag{20a}$$

$$\sigma_i = C_{ij}\epsilon_j - e_{ki}E_k \tag{20b}$$

where the contracted notation for the strain, stress, elastic modulus, and piezoelectric modulus tensors has been used [25]. The elastic constants of GaN are typically reported in terms of the stiffness tensor C_{ij} from Brillouin scattering [44], surface acoustic wave [45], or bulk acoustic wave [37] experiments. Perhaps the most commonly cited reference for the elastic constants is that of Polian *et al.* (1996) [44] of a single crystal GaN needle with uncertainties of 10 to 20 GPa in the reported values. More recent measurements of the elastic constants on bulk GaN crystals grown by the ammonothermal method [37] report values in good agreement with Polian *et al.* (1996) but with uncertainties less than 1 GPa. Values of the elastic constants from three references are listed in Table II. A more exhaustive list of references including elastic constants determined from first principles calculations is available in Ref. [37]. As shown in Table II, the values reported by Witczak *et al.* (2015) [37] have the lowest measurement uncertainty and agree to within 10% with the values previously reported by Polian *et al.* (1996) [44], which were available at the time of publication of a number of early reports on inverse piezoelectric strain in GaN HEMTs [8], [12]-[14].

TABLE II. Elastic stiffness constants C_{ij} for wurtzite GaN (GPa).

Reference	C_{11}	C_{12}	C_{13}	C_{33}	C_{44}
Polian *et al.* [44]	390 ± 15	145 ± 20	106 ± 20	398 ± 20	105 ± 10
Soluch *et al.* [45]	345 ± 10	128 ± 5	129 ± 5	430 ± 10	96.5 ± 2
Witczak *et al.* [37]	366.9 ± 0.4	135.0 ± 0.6	97.5 ± 0.2	398.1 ± 0.6	99.1 ± 0.2

In contrast, values for the piezoelectric constants for wurtzite GaN vary significantly more among different references in the literature with higher measurement uncertainty than the elastic constants. Furthermore, some references report the piezoelectric strain moduli d_{ij} and others the piezoelectric stress moduli e_{ij} requiring use of a set of the elastic constants to convert between the two forms [25]

$$d_{ki} = e_{kj}s_{ji} \tag{21a}$$
$$e_{ki} = d_{kj}C_{ji} \tag{21b}$$

Some differences in the reported values of the piezoelectric constants occur because of different measured or calculated values of the elastic stiffness or susceptibility constants appearing in Equations (21a) and (21b). A summary of the piezoelectric moduli values given in four references are shown in Table III. As in the case of the elastic constants, a more exhaustive review of values in the literature is given in Ref. [37]. All of the values of the piezoelectric stress and strain moduli from these four references differ by less than 20% from the most recent values published for bulk ammonothermal GaN crystals [37], except for the value of d_{31} from Ref. [45]. Some of the earliest values for the piezoelectric strain moduli d_{31} and d_{33} calculated from first principles by Bernardini *et al.* (2002) [47] used in the analysis of the experimental data by Sarua *et al.* (2006) [12] specifically are within 15% of the values measured recently by Witczak *et al.* (2015) [37], which themselves have low measurement uncertainties. Hence, we believe that uncertainty in the values of the elastic and piezoelectric constants available prior to 2006 are not a major factor in the uncertainty of the strain and stress values obtained by micro-Raman spectroscopy.

TABLE III. Piezoelectric stress moduli e_{ij} (C/m^2) and strain moduli d_{ij} (pm/V). Values calculated from reported values are shown in brackets. Calculated uncertainties in the piezoelectric constants here do not factor in uncertainties in the elastic constants.

Reference	e_{31}	e_{33}	d_{31}	d_{33}
Ambacher et al. [20]*	-0.49	0.73	[-1.4]	[2.6]
Bernardini et al. [47]*	[-0.36]	[0.82]	-1.2	2.4
Soluch et al. [45]	-0.47 ± 0.03	0.84 ± 0.04	[-1.8 ± 0.1]	[3.0 ± 0.1]
Witczak et al. [37]	-0.41 ± 0.04	0.86 ± 0.04	[-1.4 ± 0.1]	[2.8 ± 0.1]

* Piezoelectric moduli for Ambacher et al. [20] and Bernardini et al. [47] were calculated from elastic constants from Polian et al. [44] to be consistent with older published data.

B. Phonon Deformation Potentials

Potential deformation theory asserts that displacement of the atoms in a crystal from their equilibrium positions results in a change in the interatomic potential [33]. In phonon dynamics, strain changes the interatomic force constants atoms feel at the strained equilibrium positions due to the inherent anharmonicity of the interatomic potential distribution. If the change in phonon frequencies are approximately linear with strain in the limit of small strain values, the change in phonon frequency can be related to strain components *via* the phonon deformation potentials (PDPs). For the E$_2$ high and A$_1$ (LO) modes in wurtzite GaN, these relationships take the form of Equations (7a) and (7b) due to symmetry considerations of the wurtzite structure. Determination of the IPE-induced strain values from micro-Raman spectroscopy measurements of the changes in Stokes peak positions requires accurate knowledge of the values of the PDPs a, b, and c for the E$_2$ high and A$_1$ (LO) modes. It is important to note that potential deformation theory asserts that phonon frequency changes are fundamentally related to strain rather than mechanical stress alone.

Any physical mechanism, such as mechanical stress, electric field, and temperature rise, that induces strain results in a phonon frequency shift.

The PDPs of wurtzite GaN have been measured with a variety of techniques or calculated from first principles in the literature. The most popular experimental methods are to measure the changes in the Stokes peak position for each mode while applying a mechanical stress to a single GaN template or crystal [8],[43],[46],[48] or by analyzing GaN epilayers with different amounts of residual strain [27],[43],[49]. In the case of mechanical loading, the PDPs are determined by first measuring the dependence of the Stokes peak position on one or more stress components and then relating the stress components to the strain components. Combining the elastic constitutive relations

$$
\begin{bmatrix} \sigma_{xx} \\ \sigma_{yy} \\ \sigma_{zz} \end{bmatrix} = \begin{bmatrix} C_{11} & C_{12} & C_{13} \\ C_{12} & C_{11} & C_{13} \\ C_{13} & C_{13} & C_{33} \end{bmatrix} \begin{bmatrix} \epsilon_{xx} \\ \epsilon_{yy} \\ \epsilon_{zz} \end{bmatrix} \tag{22}
$$

with the dependence of the Stokes peak positions on strain in Equations (7a) and (7b) and assuming symmetric in-plane strain ($\epsilon_{xx} = \epsilon_{yy}$), symmetric in-plane stress ($\sigma_{xx} = \sigma_{yy}$) and negligible shear strain in the xy-plane yields the expression for the Stokes peak shift

$$
\Delta\omega_{stress} = 2\tilde{a}\sigma_{xx} + \tilde{b}\sigma_{zz} \tag{23}
$$

in terms of the stress PDPs $\tilde{a}$ and $\tilde{b}$ [46]. Equation (23) applies to both the E_2 high and A_1 (LO) modes. Determination of the strain PDPs a and b from the measurements of the Stokes line position with stress

$$
a = \tilde{a}(C_{11} + C_{12}) + \tilde{b}C_{13} \tag{24a}
$$
$$
b = 2\tilde{a}C_{13} + \tilde{b}C_{33} \tag{24b}
$$

requires that both stress PDPs $\tilde{a}$ and $\tilde{b}$ are known [46]. The quantities typically reported in the literature are the stress coefficients K according to the expression

$$\Delta\omega_{stress} = K\sigma \tag{25}$$

for (i) uniaxial stress along the c-axis $K^I = \tilde{b}$, (ii) biaxial stress in the c-plane $K^{II} = 2\tilde{a}$, and (iii) isotropic stress $K^{III} = 2\tilde{a} + \tilde{b}$. Two of the three stress coefficients (K^I, K^{II}, and K^{III}) must then be measured to determine the stress and strain PDPs. In Table IV, we summarize the values of the stress coefficients measured in several references in the literature for wurtzite GaN.

TABLE IV. Phonon frequency stress coefficients for the E_2 high and A_1 (LO) modes in wurtzite GaN (cm^{-1}/GPa).

Reference	Coefficient	E_2 high	A_1 (LO)
G. Callsen *et al.* [46]	K^I	-1.38 ± 0.10	-1.97 ± 0.22
S. Choi *et al.* [43]	K^{II}	-3.09 ± 0.41	-2.14 ± 0.28
A. Goñi *et al.* [48]	K^{III}	-4.24 ± 0.03	-4.4 ± 0.1

In this work, we calculated the strain PDPs for the E_2 high and A_1 (LO) modes in wurtzite GaN from the three stress coefficients given in Table IV according to Equations (24a) and (24a). The values of the stress PDPs were calculated from two of the three stress coefficients taken at a time. The resulting values of the strain PDPs calculated with the elastic constants from Ref. [44] along with additional values from other reports in the literature are given in Table V. The strain PDPs derived from the stress coefficients from different references [43],[46],[48] agree to within 10% of each other. There is a greater difference between the strain PDPs obtained from the stress coefficients and earlier residual stress analysis [49] and first principles calculations [50] of up to

≈25%. We note that all of the strain PDPs for both the E_2 high and A_1 (LO) modes are negative and the strain PDPs for the A_1 (LO) mode calculated from the different references agree to within the measurement uncertainties despite the lower intensity of the A_1 (LO) Stokes line in Raman measurements. As we discuss further in Section V, we believe that uncertainties in the PDPs are not a likely source of the discrepancy between measured and expected strain and stress component values as the PDPs measured by different groups and different methods agree quite closely.

TABLE V. Strain phonon deformation potentials (PDPs) of the E_2 high and A_1 (LO) modes in wurtzite GaN (cm^{-1}). Uncertainties calculated for the strain PDPs do not include the contribution from uncertainties in the elastic constants [44].

Reference/Method	a_{E_2}	b_{E_2}	a_{A_1}	b_{A_1}
K^I [46] and K^{II} [43]	-973 ± 110	-877 ± 59	-781 ± 78	-1011 ± 92
K^I [46] and K^{III} [48]	-911 ± 30	-852 ± 41	-859 ± 69	-1042 ± 91
K^{II} [43] and K^{III} [48]	-948 ± 118	-785 ± 169	-812 ± 81	-1126 ± 122
J.-M. Wagner *et al.* [50]	-740	-727	-663	-877
F. Demangeot *et al.* [49]	-850 ± 177	-963 ± 220	-782 ± 174	-1181 ± 245

V. Analysis of the Experimental Data

A. E₂ High Peak Position

Because the E_2 high mode is the highest intensity Raman peak of the allowed optical phonon modes in wurtzite GaN in the backscattering configuration, the earliest experimental studies of IPE stress and strain in the pinched OFF state utilized data primarily from the E_2 high mode [12],[14]. Assuming that the in-plane strain components ϵ_{xx} and ϵ_{yy} are negligible compared to the out-of-plane strain ϵ_{zz} because the substrate mechanically clamps the GaN buffer from

below, the full expression relating the change in E_2 high peak position to the strain components in Equation (7a) can be greatly simplified to

$$\Delta\omega_{E_2} \approx b_{E_2}\epsilon_{zz} \tag{26}$$

Thus, the out-of-plane strain ϵ_{zz} can be uniquely determined from experimental measurements of the change in E_2 high line position given the value of the strain PDP b_{E_2}. Assuming that the out-of-plane stress σ_{zz} is negligible due to free expansion of the GaN buffer in the z-direction and supported by the electro-mechanical model in Section III. B., the magnitude of the vertical electric field is determined uniquely by Equation (19) from the out-of-plane strain. Finally, the in-plane stress can be computed from the out-of-plane strain by making use of Equation (19) and the stress form of the constitutive relation in Equation (20b)

$$\sigma_{xx} \approx \left(C_{13} - C_{33}\frac{e_{31}}{e_{33}}\right)\epsilon_{zz} \tag{27}$$

Figure 6 shows the experimental values of the change in E_2 high peak position extracted from the measurements in Ref. [12] averaged over a 1 µm region to the left of the drain contact in the gate-drain access region and the out-of-plane strain, in-plane stress, and vertical electric field values calculated using the procedure described above. The error bars in the measured E_2 high peak position changes represent the standard deviation of the measurements within the 1 µm region and are propagated through the calculated values of strain, stress, and electric field, not including the small uncertainties in the material properties for simplicity. Values of the elastic and piezoelectric constants were taken from Ref. [37] and the strain PDP value b_{E_2} = -852 cm^{-1} [46] was used to calculate the out-of-plane strain. We also plotted the depth-averaged out-of-plane strain, in-plane stress, and vertical electric field values extracted from the electro-mechanical

model described in Section III. B at 0.5 µm to the left of the drain contact for the same values drain

bias values.

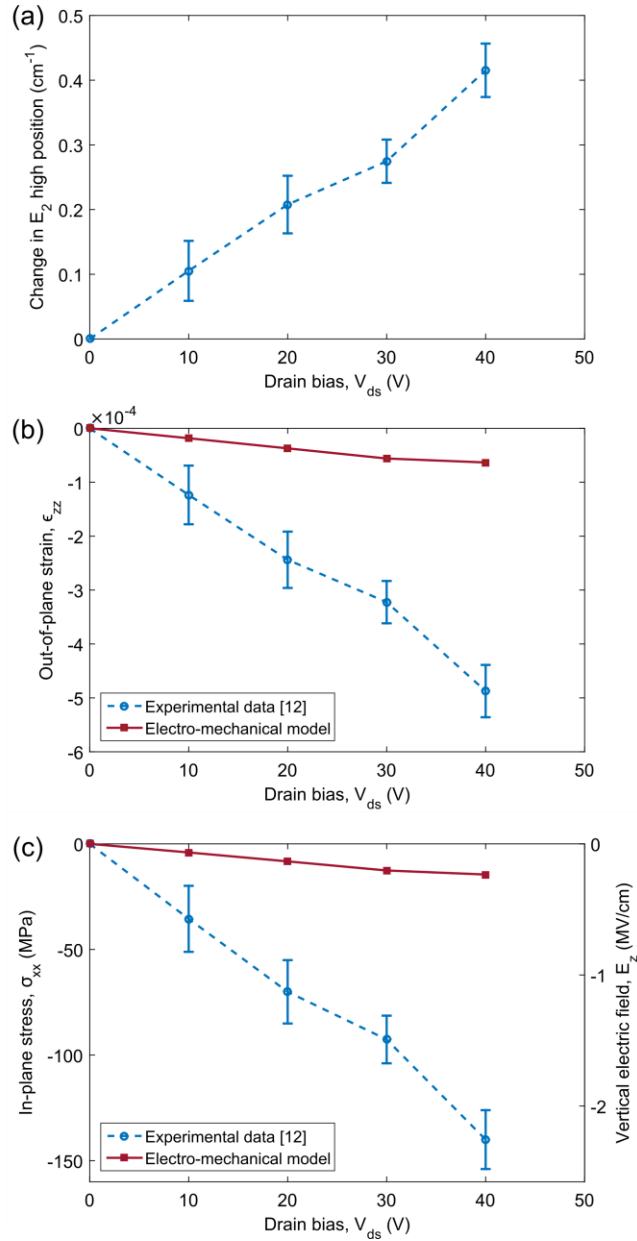FIG. 6. (a) Measured change in E_2 high peak position averaged over a 1 µm region to the left of the drain contact in the gate-drain access region, (b) out-of-plane strain ϵ_{zz}, (c) in-plane stress σ_{xx} and vertical electric field E_z extracted from experimental data [12] and our electro-mechanical model in Silvaco ATLAS/BLAZE and COMSOL Multiphysics.

The experimental data from Ref. [12] reproduced in Figure 6 (a) show an increasing change in E_2 high peak position with drain bias up to 0.42 cm^{-1} at $V_{ds} = 40$ V. In that study, the authors reported that the leakage current in the pinched OFF state was kept below 0.3 mA, which would have resulted in a dissipated power level below $\approx$0.25 W/mm, a temperature rise of less than 2 °C, and a E_2 high peak shift of less than -0.03 cm^{-1} based on estimates from Refs. [4],[9]. The calculated out-of-plane strain, in-plane stress, and vertical electric field values shown in Figure 6 (b) and (c) have corresponding magnitudes of -4.9 $\times$ 10^{-4}, -140 MPa, and -2.3 MV/cm, respectively, at $V_{ds} = 40$ V. The slight change in slope of the modeled data in Figure 6(b) and (c) occurs after $V_{ds} = 30$ V when the space charge region of filled acceptor-type traps extends throughout the GaN buffer. Although these experimental values have the same signs as the quantities predicted by the electro-mechanical model, the experimental values are an order of magnitude larger than the modeled values as was also discussed by Sarua *et al.* (2006) [12]. It is important to evaluate in detail the reasons for this serious discrepancy between measured and modeled values of the strain, stress, and electric field. Based on several hypotheses suggested by Sarua *et al.* (2006) [12] and Beechem *et al.* (2009) [14], we examine here the possibility of (i) uncertainty in the values of the material properties, (ii) quantum mechanical (non-classical) coupling between the strain components and electric field, and (iii) measured strain/stress components being related to the peak vertical electric field.

First, the uncertainty in the out-of-plane stress values derived from the experimental measurements *via* Equation (26) depend only on the uncertainty in the strain PDP b_{E_2}, which we have concluded in Section IV. B. varies less than 20% among recent values reported in the literature. The most striking quantitative discrepancy between the measured and modeled quantities is in the vertical electric field component E_z because the depth-averaged vertical electric

field in the GaN buffer, to the first order, is expected to be the drain bias divided by the thickness of the GaN buffer as long as the buffer is not fully depleted. According to Equation (19), the vertical electric field values depend on the ratio C_{33}/e_{33}, which varies from 462 GV/m [37] to 545 GV/m [20],[44] or ≈20% between different published values. The in-plane stress σ_{xx} is quite sensitive to the ratio e_{31}/e_{33} found in Equation (27), which varies as much as ≈50% between its different values of -0.44 [47], -0.48 [37], -0.56 [45] and -0.67 [20] reported in the literature. Using the values of e_{31}/e_{33} with the greatest difference of -0.44 and -0.67 to calculate the in-plane stress results in a difference of only 33% in σ_{xx}, which is always an order of magnitude greater than the modeled value. Thus, we believe it is highly unlikely that uncertainty in these material properties are responsible for the order of magnitude disagreement in the strain, stress, and electric field values extracted from the experimental data and the electro-mechanical model.

It has also been suggested that quantum mechanical coupling between the strain components, electron concentration, and polarization fields in the AlGaN/GaN heterostructure studied theoretically [51] could be responsible for this quantitative discrepancy, *i.e.*, classical elasticity and piezoelectric theory cannot capture the electro-mechanical behavior in GaN HEMTs [12]. While this may be true for the AlGaN barrier with strain values of ~10^{-3}, we do not believe it is a significant effect for the GaN buffer whose out-of-plane strain ϵ_{zz} values of ~10^{-5} to ~10^{-4} shown in Figure 5 (b) are significantly lower than the residual strain in the barrier. Very good quantitative agreement between the thermoelastic stresses in ungated and gated GaN HEMTs in the ON state measured and modeled by two studies [9],[14] also supports our hypothesis that classical continuum mechanics are sufficient to describe the behavior of the GaN buffer to the leading order. Finally, we note that using the peak vertical electric field value at the top of the GaN buffer from the electro-mechanical model would yield much better quantitative agreement between

the measured and modeled stress and strain values than those shown in Figure 6(b) to (d). However, as we have discussed previously in Section III. B., this would violate the constitutive relations expressed in Equations (4) and (14) and does not coincide with the strain and stress values predicted by our electro-mechanical model. Thus, we conclude that these hypotheses suggested by previous reports are not sufficient to explain the order of magnitude discrepancy between measured and modeled strain, stress, and electric field values.

B. A$_1$ (LO) Peak Position

The preceding analysis of the change in E$_2$ high Stokes peak position with drain bias in GaN HEMTs reported in Refs. [12]-[14] results in unsatisfactory agreement between measured and predicted strain, stress, and electric field values despite improved values of the material properties in recent years. As was first recognized by Sarua *et al.* (2006) [12], however, there is an even more serious inconsistency associated with the measured change in the A$_1$ (LO) Stokes peak position with increasing drain bias. Whereas the E$_2$ high mode frequency increases with increasing drain bias, the A$_1$ (LO) mode frequency has been observed to decrease [12]-[13]. Assuming that the in-plane strain components ϵ_{xx} and ϵ_{yy} are negligible with respect to the out-of-plane strain ϵ_{zz}, an expression analogous to Equation (26) for the E$_2$ high mode also applies to the A$_1$ (LO) mode. Noting that the strain PDP value b_{A_1} in Table V is also negative, one would expect that the A$_1$ (LO) frequency shift be positive for negative out-of-plane strain values associated with a negative vertical electric field in the gate-drain region. This is contrary to experimental measurements in GaN HEMTs on a variety of substrates with different buffer doping profiles [13] and raises serious questions regarding the applicability of the analysis outlined in the previous section.

The most complete set of measurements available in the literature for the change in both the E_2 high and A_1 (LO) positions are given by Sarua *et al.* (2010) [13]. The authors report the phonon frequency shifts with applied bias for a pair of mesa-isolated, ohmic contact pads on an AlGaN/GaN-on-SiC structure, which displays similar behavior to the gate-drain access region of a lateral HEMT but allows a higher applied bias. Given the measured changes in phonon frequency for both modes, the in-plane and out-of-plane strain components can be calculated by Equation (12) for which we use the strain PDPs reported in Ref. [46]. This analysis does not make any assumptions *a priori* about the magnitude of the in-plane strain components except that $\epsilon_{xx} = \epsilon_{yy}$ and is thus more general than the fully clamped analysis in Section V. A. Assuming that the out-of-plane stress σ_{zz} is still negligible with respect to the in-plane stress components $\sigma_{xx} = \sigma_{yy}$, the in-plane stress and vertical electric field may be calculated self-consistently using Equation (13). In Figure 7, the measured changes in phonon frequencies for the E_2 high and A_1 (LO) modes along with the normal strain components, in-plane stress, and electric field are shown using the elastic and piezoelectric constants from Ref. [37] and the strain PDPs from Ref. [46].
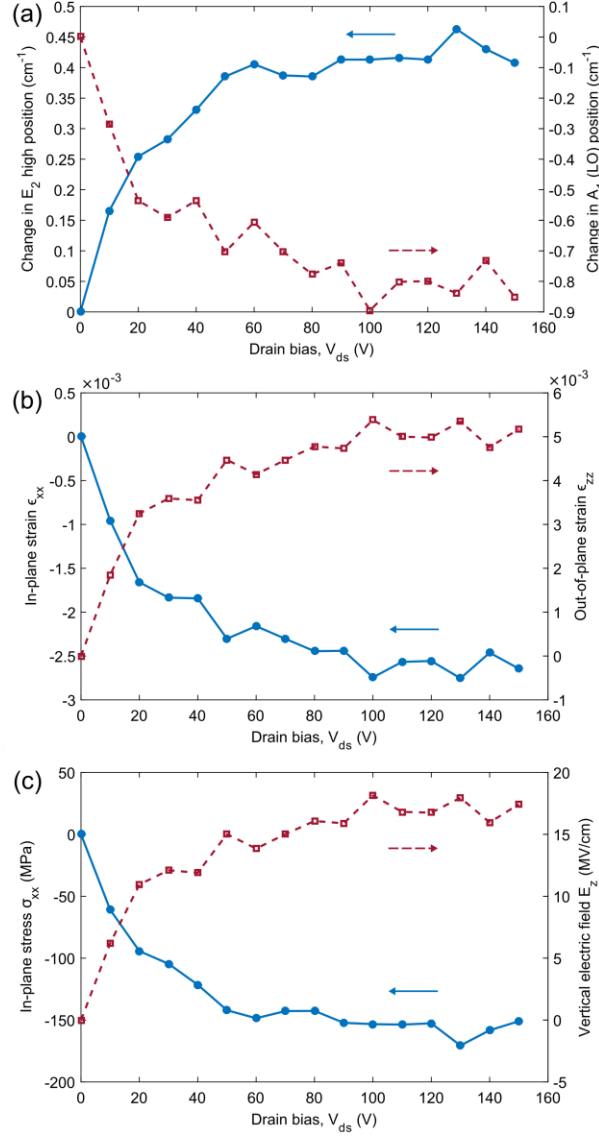
FIG. 7. (a) Measured changes in the E_2 high and A_1 (LO) Stokes peak positions, (b) derived in-plane and out-of-plane strain components, and (c) derived in-plane stress and vertical electric field.

As shown in Figure 7, the E_2 high and A_1 (LO) line positions increase and decrease sharply, respectively, up to an applied bias of ≈ 50 V, after which the further change in line positions is less rapid. This is likely due to the full depletion of the GaN buffer due to the relatively low impurity (acceptor-type trap) concentration of $(3.0 \pm 0.5) \times 10^{-16}$ cm^{-3} in this particular buffer structure [13]. Correspondingly, the in-plane and out-of-plane strain components increase in magnitude from zero

to their saturation values at high applied drain biases. The magnitudes of the in-plane and out-of-plane strain components at an applied bias of 40 V, for instance, are -1.9×10^{-3} and 3.5×10^{-3}, respectively, which is an order of magnitude higher than the value of -4.9×10^{-4} derived from the E_2 high analysis in the previous section. Furthermore, we find that the difference in sign between the values of the out-of-plane strain ϵ_{zz} determined from the experimental measurements of the E_2 high only and E_2 high/A_1 (LO) analysis leads to a difference in sign for the vertical electric field. At an applied bias of 40 V, the in-plane stress and vertical electric field have magnitudes of -120 MPa and 11.8 MV/cm, respectively. The sign of the in-plane stress actually matches the expected direction (compressive) of the in-plane stress from the electro-mechanical model though it is still an order of magnitude higher than the expected range. The derived value of the vertical electric field, however, has the wrong sign (positive) and its magnitude is two orders of magnitude higher than the expected average vertical electric field and at least one order of magnitude higher than the peak vertical electric field in the GaN buffer. We finally note that the ratio of the derived in-plane to out-of-plane strain values $\epsilon_{xx}/\epsilon_{zz}$ at 40 V is surprisingly high with a value of -0.54 considering that the in-plane strain is predicted to be one order of magnitude lower than the out-of-plane strain by the electro-mechanical model if the bottom surface of the GaN buffer is rigidly clamped by the substrate.

In the analysis of the measured changes in the E_2 high and A_1 (LO) peak positions, the strain components ϵ_{xx} and ϵ_{zz} are uniquely determined by the matrix of strain PDPs in Equation (12). Although using different sets of strain PDPs from the literature listed in Table V strongly affects the quantitative values of ϵ_{xx} and ϵ_{zz} derived from measurements, the signs ($\epsilon_{xx} < 0$ and $\epsilon_{zz} > 0$) and order of magnitude ($\sim 10^{-3}$) remain the same as in Figure 7. On the other hand, the derived values of the in-plane stress σ_{xx} and the vertical electric field component E_z depend on

the elastic and piezoelectric constants according to Equation (13). Different values of the piezoelectric moduli d_{31} and d_{33} can change the magnitude of σ_{xx} from ≈-200 MPa (compressive) to ≈100 MPa (tensile) for $V_{ds} \geq 50$ V. The vertical electric field depends more strongly on the elastic constants than the piezoelectric constants and thus changes magnitude from ≈10 MV/cm to ≈20 MV/cm at high applied bias but always remains positive. Therefore, we believe that uncertainties in the strain PDPs and elastic and piezoelectric constants are not able to account for the discrepancies in the vertical electric field and IPE-induced strain components between measured and modeled values. Despite our best efforts to understand the electro-mechanical behavior of the GaN buffer and most accurate values of the material properties of GaN available in the literature, we find that the E$_2$ high/A$_1$ (LO) analysis yields even more drastic disagreement between measured and modeled strain, stress, and electric field values.

C. Additional Considerations

1. Non-uniform Optical Sampling

In this review, we have assumed that the strain, stress, and electric field values derived from changes in the Raman peak positions represent the average values of those quantities calculated by the average value theorem $\bar{u} = \frac{1}{L}\int_{-L}^{L} u(z)dz$ through the thickness of the GaN buffer. This has also been assumed in almost every report in the literature on micro-Raman thermometry of GaN HEMTs in which the changes in Raman peak positions are correlated to the average temperature rise of the GaN buffer [2]-[10]. In many of these studies, the average temperature rise of the buffer calculated from numerical heat transfer models has shown good agreement with the temperature rise derived from micro-Raman measurements under this assumption. To further support this assumption, Beechem (2008) simulated the Raman spectrum response to temperature

gradients across the GaN buffer as large as 50 °C and found that the temperature values derived from the changes in Raman peak position agreed to within 1 °C of the average temperature of the buffer [42]. Because the vertical electric field, strain, and stress vary significantly with depth in the GaN buffer when a GaN HEMT is biased in the pinched OFF state, it is worthwhile to also consider the possibility of non-uniform optical sampling of different depths into the buffer by micro-Raman spectroscopy in this work. If the Raman spectrum were preferentially weighted toward the top of the buffer where the IPE-induced strain is the highest, this effect might account for some of the discrepancy between modeled and measured values of the IPE-induced strain and stress.

The aggregate Raman spectrum collected from the buffer by the microscope objective and imaged by the spectrograph is a sum of the Raman spectrum from each z slice through the thickness of the buffer. Under the assumption that the depth of field extends through the thickness of the buffer, the Raman spectrum at each z slice could differ because of at least three effects: (i) non-uniform laser intensity in the buffer, (ii) changes in the Raman peak position and linewidth due to the strain, stress, and electric field at that location, (iii) changes in the Raman scattering efficiency also due to the local strain, stress, and electric field. Thus, the aggregate Raman spectrum may be written as

$$I_s(\omega) = \int_{-L}^{0} I_0(z)S(z)L(\omega, z; \mu, \Gamma)dz \tag{28}$$

where $I_0(z)$ is the laser intensity, $S(z)$ is the Raman scattering efficiency (related to the number of photons converted from the laser line to the Raman scattered light) [52], and $L(\omega, z; \mu, \Gamma)$ is the normalized Lorentzian lineshape associated with the intrinsic Raman spectrum. The Lorentzian lineshape is given by

$$L(\omega, z; \mu, \Gamma) = \frac{\Gamma}{2\pi} \frac{1}{(\omega - \mu)^2 + (\Gamma/2)^2} \tag{29}$$

where μ is the centroid and Γ is the linewidth or full width at half maximum (FWHM) [18]. Based on Equations (7a) and (7a), we can model the response of the Raman spectrum of each z slice as a local change in the Lorentzian centroid μ associated with the local strain components $\epsilon_{ij}(z)$. It has been shown experimentally that the linewidth Γ of the E_2 high peak decreases with increasing drain bias in the pinched OFF state, which can be understood in terms of either the associated IPE-induced strain or the IPE-induced stress and vertical electric field [5],[8]. However, there has been little theoretical work to quantitatively explain how the E_2 high linewidth depends on the strain, stress, and electric field components. Similarly, the change in Raman scattering efficiency due to changes in strain, stress, and electric field is difficult to quantify. For the purposes of estimating the impact of non-uniform optical sampling here, we assume the E_2 high linewidth and Raman scattering efficiency are constant throughout the GaN buffer.

The laser intensity as a function of depth $I_0(z)$ in the buffer could be influenced by a variety of factors, including absorption in the buffer and thin film interference in the GaN-on-SiC epilayer structure. From a simple model of light absorption, the laser intensity should decay exponentially with depth into the GaN buffer according to $I_0(z) = I_0(0)e^{-\alpha z}$, where α is the absorption coefficient [53]. Due to the fact that GaN has a wide bandgap of 3.43 eV [54], the absorption coefficient is very low at sub-bandgap, visible laser wavelengths of 488 nm to 633 nm (2.54 eV to 1.96 eV). Although it is difficult to obtain quantitative values of the absorption coefficient at 488 nm from the literature because it is near zero [54]-[55], we can conservatively estimate $\alpha = 0.1$ µm⁻¹, corresponding to an optical penetration depth $\delta = 1/\alpha$ of 10 µm. Then, laser intensity at the bottom of the 1.2 µm buffer analyzed in Section V would be reduced to 89% of its value at the top

of the buffer. If wurtzite GaN is less absorptive at visible wavelengths, the laser intensity would be even more uniform than this throughout the thickness of the buffer. Owing to the fact that the epilayers in the HEMT structure are films with thicknesses typically less than 2 µm, there is also the possibility of thin film interference effects leading to intensity fringes in the GaN buffer. To address this issue, we calculated the 1D laser intensity profile for the GaN-on-SiC epilayer structure described in Section III. A (30 nm $Al_{0.25}Ga_{0.75}N$, 1.2 µm GaN, 100 nm AlN, and 100 µm 4H-SiC) using the optical transfer matrix formalism [56] and indices of refraction at 488 nm reported in the literature [57]-[58]. As a conservative approximation, we also set the absorption coefficient of each layer equal to $\alpha = 0.1$ µm^{-1}. The calculated intensity profile in the GaN buffer shows interference fringes with a period of 110 nm and a peak-to-peak intensity variation of 16% due to multiple reflections from the layers on both sides of the buffer.

We can directly compare the assumption that the Raman peak shifts are correlated to the average strain components and the effect of non-uniform optical sampling by evaluating the integral in Equation (28) with the electro-mechanical model described in Section III. B. We extracted the normal strain components ϵ_{xx}, ϵ_{yy}, and ϵ_{zz} through the depth of the GaN buffer alone a line 0.5 µm to the left of the drain contact in the gate-drain access region at $V_{ds} = 20$ V and $V_{gs} = $ -6 V. Then, we used Equation (7a) to compute the shift of the E$_2$ high mode (neglecting the asymmetric third term for simplicity) with the strain PDPs $a_{E_2} = $ -911 cm^{-1} and $b_{E_2} = $ -852 cm^{-1} [46] as the centroid of the Lorentzian μ at each location with a fixed linewidth of $\Gamma = 3$ cm^{-1}. With the simple laser intensity profile of $I_0(z) \sim e^{-\alpha z}$ and $\alpha = 0.1$ µm^{-1}, we evaluated Equation (28) and found that the E$_2$ high mode shifted positively by $\Delta \omega_{E_2} = 0.027$ cm^{-1} by fitting a Lorentzian lineshape to the simulated aggregate Raman spectrum. Including the periodic variation in laser intensity associated with thin film interference effects in Equation (28) also resulted in a Raman

peak shift of $\Delta\omega_{E_2} = 0.027$ cm^{-1}. This is almost identical to the E$_2$ high mode shift of $\Delta\omega_{E_2} = 0.026$ cm^{-1} predicted by using the average strain values $\bar{\epsilon}_{ij} = \frac{1}{L}\int_{-L}^{L}\epsilon_{ij}(z)dz$ extracted from the electro-mechanical model at the same bias point and Equation (7a). Both values are an order of magnitude lower than the experimentally observed value of $\Delta\omega_{E_2} = 0.21$ cm^{-1} reported by A. Sarua *et al.* (2006) [4] for the device simulated by our electro-mechanical model. We also found that allowing the E$_2$ high linewidth to vary linearly from $\Gamma = 2$ cm^{-1} to 3 cm^{-1} from the top to the bottom of the GaN buffer only increases the shift to $\Delta\omega_{E_2} = 0.031$ cm^{-1} in the non-uniform optical sampling case. Based on this calculation, we believe that the aggregate Raman spectrum collected in micro-Raman spectroscopy is closely related to the average strain, stress, and electric field values through the thickness of the GaN buffer and that non-uniform optical sampling of the buffer is not a primary source of the discrepancy between measured and modeled values of these quantities.

2. Phonon-plasmon Coupling of the A₁ (LO) Mode

Due to their polar characteristic, the phonon modes belonging to the A$_1$ and E$_1$ representations in wurtzite GaN are phonon-plasmon coupled modes whose phonon frequency can be strongly affected by the free electron concentration [16],[59]-[60]. The frequency of the A$_1$ (LO) phonon-plasmon (LPP) coupled mode increases with increasing free electron concentration according to the equation

$$\omega_{LPP} = \frac{1}{\sqrt{2}}\left\{\omega_{LO}^2 + \omega_p^2 + \left[\left(\omega_{LO}^2 + \omega_p^2\right)^2 - 4\omega_p^2\omega_{TO}^2\right]^{\frac{1}{2}}\right\}^{1/2} \tag{30}$$

where ω_{LO} and ω_{TO} are the uncoupled A_1 (LO) and A_1 (TO) phonon frequencies, respectively, and ω_p is the uncoupled plasma frequency [60]. This uncoupled plasma frequency in wavenumber SI units (m^{-1}) is given by

$$\omega_p = \frac{1}{2\pi c} \sqrt{\frac{ne^2}{m^* \varepsilon_\infty \varepsilon_0}} \tag{31}$$

where c is the speed of light, n is the free electron concentration, e is the fundamental charge, m^* is the electron effective mass, ε_∞ is the high frequency dielectric constant, and ε_0 is the permittivity of free space. Experimental studies have shown that the A_1 (LO) frequency can shift, for instance, from 737 cm^{-1} at a free electron concentration of $n = 1.2 \times 10^{17}$ cm^{-3} to 740 cm^{-1} at $n = 2.2 \times 10^{17}$ cm^{-3} [16]. Because the decrease in A_1 (LO) frequency observed in GaN HEMTs in the pinched OFF state is typically less than 1 cm^{-1}, it is important to evaluate whether this phonon-plasmon coupling effect could be responsible for the shifts in the A_1 (LO) mode.

First, one should note that the changes in E_2 high and A_1 (LO) Raman peak positions discussed in this section occur primarily in the gate-drain access region and under the drain contact when the drain bias is increased and the gate bias is kept constant. While changes in the gate bias strongly change the electron concentration in the 2DEG underneath the gate, changes in the drain bias (at a fixed gate bias below the threshold voltage) only weakly affect the electron concentration in the gate-drain access region. From our Silvaco ATLAS/BLAZE model described in Section III. A., we found that the average free electron concentration through the thickness of the GaN buffer decreased from 6.02×10^{16} cm^{-3} to 4.14×10^{16} cm^{-3} as the drain bias is increased from 0 V to 40 V at a gate bias of -6 V. Using Equation (31) with the values $\omega_{LO} = 735$ cm^{-1}, $\omega_{TO} = 533$ cm^{-1}, $\varepsilon_\infty = 5.35$, and $m^* = 0.19m_0$ [16], it seems that this change in average electron concentration could

result in a decrease of the A_1 (LO) frequency from 736.72 cm^{-1} to 736.18 cm^{-1} ($\Delta\omega_{A_1}$ = -0.54 cm^{-1}), which is indeed very close to the measured shift in the A_1 (LO) frequency as the drain bias increases from 0 V to 40 V [12].

Unlike the strain, stress, and electric field discussed previously, however, the free electron concentration has a very strong effect on the linewidth of the A_1 (LO) mode. Kozawa *et al.* (1994) [59] reported that the linewidth of the A_1 (LO) mode increased from 6.7 cm^{-1} for an undoped GaN sample to 70 cm^{-1} for a heavily Si-doped GaN sample ($n = 2.5 \times 10^{18}$ cm^{-3}). To capture this effect, we calculated a simulated aggregate Raman spectrum using Equation (28) with the electron concentration $n(z)$ extracted from the Silvaco ATLAS/BLAZE model at drain biases of $V_{ds} = 0$ V and 40 V and a gate bias of V_{gs} = -6 V and extracted the A_1 (LO) frequency shift by fitting the simulated spectrum to a Lorentzian lineshape. The linewidth Γ of the Lorentzian lineshape at each z slice was interpolated from the reported linewidths in Ref. [59] based on the local free electron concentration from the model, and an optical absorption coefficient of $\alpha = 0.1$ µm^{-1} was used. With this more detailed calculation, we found that the A_1 (LO) frequency changed by a much smaller value of $\Delta\omega_{A_1}$ = -0.01 cm^{-1} between these two drain bias values, which is negligible compared to the value of $\Delta\omega_{A_1} \approx$ -0.4 cm^{-1} reported by Sarua *et al.* (2006) [12]. We also calculated the change in frequency of the A1 (LO) mode to be less than -0.01 cm^{-1} when we repeated the calculation with a more detailed expression for the lineshape of the A_1 (LO) LPP coupled mode given by Equation (1) in Kozawa *et al.* (1994) [59].

Apart from this direct quantitative estimate of the effect of phonon-plasmon coupling on the A_1 (LO) frequency in this study, there are a few additional heuristic reasons to suggest it plays a minor role in micro-Raman spectroscopy of GaN HEMTs. The change in electron concentration in the buffer in the gate-drain access region discussed above is primarily a function of the drain

bias and occurs whether the channel of the HEMT is open ($V_{gs} > V_{th}$) or closed ($V_{gs} < V_{th}$). If phonon-plasmon coupling were strongly affecting the frequency of the A_1 (LO) mode in the pinched OFF state, it should also be present in micro-Raman thermometry measurements in the ON state. This seems unlikely because the simultaneous measurement of the E_2 high and A_1 (LO) Raman peaks to uncouple the effects of thermoelastic stress and temperature rise has shown very good agreement with thermo-mechanical models [7],[9]. In addition, Sarua *et al.* (2006) [4] found that the A_1 (LO) peak position measured directly under the gate (where the electron concentration is expected to change the most) did not change with changing gate bias to within experimental uncertainty. Rather, the A_1 (LO) peak was found to shift primarily in the gate-drain access region and under the drain contact where the E_2 high peak also shifted the most. This suggests that the A_1 (LO) frequency changes in response to the strain, stress, and electric field rather than the electron concentration because the frequency of the non-polar E_2 high mode is not affected by changes in the electron concentration. Thus, we conclude that phonon-plasmon coupling of the A_1 (LO) mode is not the dominant factor causing the negative shift of the A_1 (LO) Raman peak.

VI. Open Research Questions

A. Dependence on Buffer Impurity Concentration

Thus far, we have primarily discussed the change in Raman peak positions of unintentionally doped (UID) GaN buffer layers on SiC substrates in the pinched OFF state. Sarua *et al.* (2010) reported that AlGaN/GaN HEMTs fabricated on buffer layers with different doping profiles on different substrates exhibited different coefficients of phonon frequency shifts with drain bias [13]. The undoped or unintentionally doped (UID) GaN buffer layer with an approximately uniform impurity density of $(3.0 \pm 0.5) \times 10^{-16}$ cm^{-3} showed the largest coefficients

of 0.01 cm^{-1}/V and -0.017 cm^{-1}/V for the E$_2$ high and A$_1$ (LO) modes, respectively. For much more highly iron-doped buffer layers on SiC and unspecified doping levels on sapphire and silicon substrates, the same coefficients were as low as 0.003 cm^{-1}/V and -0.006 cm^{-1}/V, respectively. As discussed in Ref. [13], a higher impurity or trap concentration in the GaN buffer results in a narrower depletion region for the same drain bias because there is a higher amount of trapped charge to account for the change in potential difference across the buffer. The peak vertical electric field across the narrower depletion region also increases with increasing impurity concentration. Therefore, it has been suggested that increasing the doping concentration concentrates the electric field near the top surface of the GaN buffer and induces lower stress/strain magnitudes measured by micro-Raman spectroscopy because an increasingly large portion of the GaN buffer remains mechanically unaffected between the zero bias and pinched OFF states.

Although changes in the impurity concentration in the buffer do significantly change the vertical electric field profile along the z-axis, $E_z(z)$, the average vertical electric field across the GaN buffer is always the difference in electric potential across the buffer divided by the thickness of the buffer. Using the 1-D form of Gauss' law and Equation (15), one can show that the average vertical electric field in the GaN buffer is related to the total space charge $\int_{-L}^{0} \rho(z)\, dz$ and is independent of the functional form of the space charge $\rho(z)$. As long as the impurity concentration and buffer thickness are high enough so that the buffer is not fully depleted, the depth-averaged vertical electric field is essentially independent of the impurity concentration. Based on the results of our electro-mechanical model and the depth-averaged constitutive relations in Equation (14), we believe that the depth-averaged values of strain and stress measured by micro-Raman spectroscopy should be directly correlated to this average vertical electric field. Thus, these mechanical quantities should also be independent of the impurity concentration. Because the

explanation suggested by Sarua *et al.* (2010) is not supported by electro-mechanical modeling, we believe that the reason for the effect of doping concentration on the phonon shift coefficient is still unknown and an important topic of further research. While one might speculate that IPE-induced stress/strain penetrates in the SiC substrate when GaN buffer layers with low impurity concentration are fully depleted, it has been shown experimentally that the Raman peaks of SiC exhibit a negligible shift in frequency when the GaN HEMT is in the pinched OFF state, suggesting negligible stress/strain in the SiC substrate [13].

B. Raman Peak Linewidth

In addition to the changes in the positions of the E_2 high and A_1 (LO) Raman peaks, two references have reported a decrease in the E_2 high peak linewidth with increasing drain bias in the pinched OFF state [8],[13]. The linewidth or full width at half maximum (FWHM) of the Stokes peak is a convolution of the intrinsic Raman spectrum of that optical phonon mode and the instrumental response of the spectrometer used to capture the Raman spectrum. With the proper deconvolution of these two features, the optical phonon lifetime can be extracted from the FWHM of the Stokes peak as the FWHM and lifetime are inversely related through the time-energy Heisenberg uncertainty relation [8]. Although it is well-known that a decrease in the FWHM of the E_2 high peak indicates an increasing lifetime of the E_2 high mode, a quantitative explanation of how the IPE-induced stress and/or strain components affect the E_2 high lifetime has not been reported.

Beechem *et al.* (2008) suggested that a change in E_2 high linewidth as much as -0.4 cm^{-1} at a drain bias of ≈50 V could be associated with a stress along the c-axis σ_{zz} induced in the pinched OFF state [8]. This argument was based on the observation that a uniaxial stress in

the c-plane applied by a four-point bending test did not result in a noticeable change in the E_2 high linewidth. However, this hypothesis was later tested directly by applying a mechanical stress along the c-axis σ_{zz}, which indicated that the E_2 high linewidth changed less than 0.1 cm^{-1} for applied σ_{zz} values from -200 MPa to 200 MPa [42]. In light of our electro-mechanical modeling work presented in this review, we do not believe there to be a significant out-of-plane stress σ_{zz} induced in the pinched OFF state and therefore conclude it is still unknown precisely why the E_2 high linewidth decreases. Due to the fact that IPE-induced strain changes the interatomic potential and force constants, it is possible that the phonon lifetimes can also be affected by strain because of anharmonicity in the interatomic potential [17],[61]. However, both computational and experimental research is needed to establish the quantitative link between the strain and stress components and observed changes in the Raman peak linewidths.

C. Non-IPE Electric Field Dependence of Phonon Frequencies

Since the experimental data reported in Ref. [13] was published in 2010, there have not been any subsequent reports, to the best of our knowledge, that have addressed the major discrepancies in strain, stress, and electric field values between measured and predicted values from electro-mechanical modeling described in Section V. While a number of hypotheses have been offered as to the reason why such discrepancies might exist, none of the hypotheses have been thoroughly investigated and shown definitively to resolve these issues. We believe that there is possibly an effect of the vertical electric field on phonon frequencies that has not been mentioned in the primary references on IPE stress/strain in GaN HEMTs [8],[12]-[14] but has been observed experimentally in strontium titanate (SrTiO$_3$) [62] and predicted theoretically for zinc blende gallium arsenide (GaAs) and aluminum arsenide (AlAs) [63]. Here, we focus our attention on the

calculations for GaAs and AlAs as these III-V semiconductors are more similar than $SrTiO_3$ in composition and structure to wurtzite GaN.

According to Wang and Vanderbilt (2006), an electric field has primarily three effects on a polar, electrically-insulating crystal, such as GaAs, AlAs, and GaN [63]. The electric field changes (i) the lattice constants or strain, which is equivalent to the IPE effect, (ii) the equilibrium atomic coordinates within the unit cell, *e.g.*, the distance between the cation and anion in III-V semiconductors, and (iii) the electronic configuration. All three factors should be expected to change the optical phonon frequencies at the Γ-point measured by micro-Raman spectroscopy as they change the interatomic potential and force constants. The strain PDPs discussed extensively in this review only account for changes of type (i) that are associated with the IPE effect. Thus, changes of type (ii) and (iii) have not been accounted for in the analysis of the changes in Raman peak positions in the pinched OFF state in GaN HEMTs nor have been demonstrated experimentally for any other III-V semiconductors to the best of our knowledge. Provided that Equation (12) properly accounts for the strain contribution to the change in E_2 high and A_1 (LO) mode frequencies, the effect of the vertical electric field on the phonon frequencies in GaN would have to be very significant to produce values of strain, stress, and electric field that agree with our electro-mechanical model. For an electric field along the [100] axis in zinc blende GaAs, Wang and Vanderbilt (2006) calculated the optical phonon frequencies at the Γ-point to shift linearly with a coefficient of up to ± 0.75 cm^{-1}/(MV/cm) [63]. This value is an order of magnitude higher than the vertical electric field coefficient for the A_1 (LO) mode in wurtzite GaN of $B_{A_1} = -0.07$ cm^{-1}/(MV/cm) given by Equation (10b) associated with the IPE effect. Although the electric field shift coefficients have not been reported for wurtzite GaN for effects of type (ii) and (iii), it is highly

possible that this effect is the missing key to the proper interpretation of the Raman peak position changes observed in the pinched OFF state in GaN HEMTs.

VII. Conclusions

The use of the pinched OFF state as a reference for micro-Raman thermography is an important experimental practice required to obtain accurate temperature measurements of GaN HEMTs in the ON state from changes in the Stokes peak positions. However, experimental characterization of the stress and strain induced in the GaN buffer by the inverse piezoelectric effect yields discrepancies of one to two orders of magnitude, often with the opposite sign, from the values predicted by electro-mechanical modeling. In light of the relatively small variation in material properties reported in the literature for wurtzite GaN and success of potential deformation theory and continuum mechanics in describing the thermo-mechanics of GaN HEMTs, we believe that an effect not mentioned in the GaN literature is a possible solution to these issues. Because it has been demonstrated theoretically via first-principles calculations for GaAs that the electric field can strongly shift the optical phonon frequencies apart from the inverse piezoelectric effect, we believe the same effect could be shifting the E_2 high and A_1 (LO) mode frequencies in the pinched OFF state in GaN HEMTs. Significant further research is needed to examine this hypothesis theoretically and experimentally as well as other features of changes in the Raman spectra, including the dependence on buffer impurity concentration and changes in the Raman peak linewidths. We anticipate that this topic will provide a deeper understanding of the electrical, thermal, and mechanical behavior of GaN HEMTs under bias for reliability analysis and an opportunity for fundamental research into the lattice dynamics of polar semiconductors.

Acknowledgements

Appendix A: Crystallographic and Transistor Coordinate Systems

Following the convention established for piezoelectric crystals [25]-[27], we must choose a particular crystallographic x,y,z coordinate system for which Equations (4), (7a), and (7b) describe the piezoelectric constitutive relation and the dependence of the Raman peak positions on the strain tensor components. In this convention, the x-axis and z-axis are chosen to be the [11-20] and [0001] directions in the wurtzite crystal structure. Then, it follows that the mutually orthogonal y-axis must be the [-1100] direction for a right-handed coordinate system. However, it is convenient to specify another x',y',z' coordinate system related to the features of the transistor. Lateral GaN HEMTs are fabricated with the c-axis or z'-axis perpendicular to the AlGaN/GaN heterojunction so it is natural to set $z' = z$. Following previous works in the literature, we then chose the x'-axis to point along the channel from the source to the drain (perpendicular to the gate) and the y'-axis to point along the gate [12]. Depending on the orientation of the transistor with respect to the crystallographic planes (marked by a wafer flat prior to fabrication), there is the

possibility that the transistor $x'y'$-plane is rotated by an angle θ counter-clockwise with respect to the crystallographic xy-plane. In the following derivation, we prove that this difference in coordinate systems does not affect the applicability of Equations (7a) to (9). We show that the tensor properties of wurtzite GaN do not change under a rotation around the z-axis and that Equations (7a) to (8) are also invariant under the same rotation.

All second order tensor material properties, such as the dielectric permittivity, of all hexagonal crystals are orthotropic with $\varepsilon_{xx} = \varepsilon_{yy} \neq \varepsilon_{zz}$ and all other components equal to zero

$$\varepsilon = \begin{bmatrix} \varepsilon_{xx} & 0 & 0 \\ 0 & \varepsilon_{xx} & 0 \\ 0 & 0 & \varepsilon_{zz} \end{bmatrix} \tag{A1}$$

in the crystallographic coordinate system. A second order tensor ε in the crystallographic coordinate system can be transformed to the transistor coordinate system ε' under the rotation transformation $R(\theta)$ by the equation [25]

$$\varepsilon'_{ij} = R_{ik} R_{j\ell} \varepsilon_{k\ell} \tag{A2}$$

Due to the fact that the diagonal second order tensor components in the xy-plane are the same and the off-diagonal components are zero, this and every second order tensor property is invariant under a rotation transformation around the z-axis ($\varepsilon' = \varepsilon$). The same relation can be proved for third order tensor properties in the xy-plane, such as the piezoelectric moduli d_{3ij} relating the strain tensor ϵ_{ij} to the vertical electric field E_z in the two coordinate systems ($d'_{3ij} = d_{3ij}$). Thus, a difference in rotation angle θ between the well-defined crystallographic axes and the convenient axes we choose because of the transistor features does not change the form nor magnitude of the tensor material properties.

The invariance of the tensor properties (matter tensors) due to a rotation by an angle θ around the z-axis is related to Neumann's principle, which states that the tensor properties of a crystal should have at least as many symmetry elements as the point group of the crystal [25]. Field tensors, such as stress σ_{ij} and strain ϵ_{ij}, however, are not invariant under rotation by an angle θ and will not be identical in the crystallographic x, y, z and transistor x', y', z' coordinate systems. Using the rotation transformation equation in Equation (A2), we transform the strain tensor ϵ_{ij} in the crystallographic coordinate system to that in the transistor coordinate system ϵ'_{ij}

$$\epsilon'_{xx} = \epsilon_{xx} \cos^2 \theta + \epsilon_{yy} \sin^2 \theta + \epsilon_{xy} \sin 2\theta \tag{A3a}$$

$$\epsilon'_{yy} = \epsilon_{xx} \sin^2 \theta + \epsilon_{yy} \cos^2 \theta - \epsilon_{xy} \sin 2\theta \tag{A3b}$$

$$\epsilon'_{xy} = \frac{1}{2}\left(-\epsilon_{xx} + \epsilon_{yy}\right) \sin 2\theta + \epsilon_{xy} \cos 2\theta \tag{A3c}$$

which explicitly shows that the strain components are not equal in the two coordinate systems. However, the applicability of the potential deformation relationships in Equations (7a) to (8) depends upon the equivalence of the quantities $\epsilon_{xx} + \epsilon_{yy}$ and $\left(\epsilon_{xx} - \epsilon_{yy}\right)^2 + 4\epsilon_{xy}^2$ in the two coordinate systems rather than the strain components ϵ_{xx}, ϵ_{yy}, and ϵ_{xy} individually. By simple algebra, it can be shown that $\epsilon_{xx} + \epsilon_{yy} = \epsilon'_{xx} + \epsilon'_{yy}$ and $\left(\epsilon_{xx} - \epsilon_{yy}\right)^2 + 4\epsilon_{xy}^2 = \left(\epsilon'_{xx} - \epsilon'_{yy}\right)^2 + 4\epsilon'^2_{xy}$ so that Equations (7a) and (7b) can be written in the transistor coordinate system

$$\Delta\omega_{E_2} = a_{E_2}\left(\epsilon'_{xx} + \epsilon'_{yy}\right) + b_{E_2}\epsilon'_{zz} \pm c_{E_2}\sqrt{\left(\epsilon'_{xx} - \epsilon'_{yy}\right)^2 + 4\epsilon'^2_{xy}} \tag{A4a}$$

$$\Delta\omega_{A_1} = a_{A_1}\left(\epsilon'_{xx} + \epsilon'_{yy}\right) + b_{A_1}\epsilon'_{zz} \tag{A4b}$$

which are identical to Equations (7a) and (7b) with unprimed variables replaced by their primed counterparts. The piezoelectric constitutive relation in Equation (4) is also the same in both the crystallographic and transistor coordinate systems since we have proven that the tensor properties of the crystal are invariant under the rotation transformation. This allows one to also express Equation (8) in the transistor coordinate system as

$$\Delta\omega_{E_2} = \left[a_{E_2}(s_{11} + s_{12}) + b_{E_2}s_{13}\right](\sigma'_{xx} + \sigma'_{yy}) + \left[2a_{E_2}s_{13} + b_{E_2}s_{33}\right]\sigma'_{zz}$$
$$\pm c_{E_2}|s_{11} - s_{12}|\sqrt{(\sigma'_{xx} - \sigma'_{yy})^2 + 4\sigma'^2_{xy}} + \left[2a_{E_2}d_{31} + b_{E_2}d_{33}\right]E'_z \qquad \text{(A5)}$$
$$+ \left[2a_{E_2}\alpha_{xx} + b_{E_2}\alpha_{zz}\right]\Delta T$$

Therefore, choosing a coordinate system x', y', z' that is related to the transistor features does not affect the interpretation of changes in the Raman spectra of the E_2 high and A_1 (LO) modes according to Equations (A5) and (9). In Section II. B., we pointed out that there should be a distinction between the crystallographic x, y, z and transistor $x', y', 'z'$ coordinate systems. In the remainder of the paper, however, we neglect this distinction and denote the transistor coordinate system with the unprimed coordinates x, y, z for convenience.

Appendix B: Separation of Inverse Piezoelectric and Thermoelastic Stresses

The applicability of the pinched OFF state as a reference in micro-Raman thermometry to determine the temperature rise in the ON state with respect to the zero bias state depends on whether the total frequency shift in Equation (9) can be decomposed into two parts as given in Equation (11a) and (11b). To be precise, the phonon frequencies of a GaN epilayer in the zero bias

state differ from the theoretical frequencies of a perfect GaN crystal with zero strain and zero electric field by (i) residual stress incurred during the epitaxial growth process and (ii) the vertical electric field due to the built-in potential across the GaN buffer. In theory, the first factor depends on the growth parameters and nucleation and stress management layers between the substrate and the buffer, and the second factor depends on the difference in bandgap and electron affinity of the epilayers and the doping/impurity concentration in the GaN buffer resulting in the equilibrium band alignment. When a bias condition is applied to the contacts of a GaN HEMT, the phonon frequencies may change due to three primary factors according to Equation (9): (i) a rise in temperature, (ii) a change in the stress state, and (iii) a change in the electric field distribution.

The application of a positive drain bias in the pinched OFF state changes the electric field distribution and induces a stress in the GaN buffer due to the IPE effect. Because there is negligible power dissipation in the pinched OFF state due to negligible drain current (<1 mA/mm), there is near zero temperature rise. Thus, the change in Raman peak position between the zero bias state and the pinched OFF state is only associated with the IPE-induced stress σ^{IPE} and pinched OFF electric field. In the ON state, however, there may be significant drain current, power dissipation, and temperature rise resulting in a thermoelastic stress in the GaN buffer due to temperature gradients and difference in coefficients of thermal expansion between the epilayers and substrate. At the same time, a positive drain bias changes the electric field distribution with respect to the zero bias state and induces an IPE-related stress. Using the difference in Raman peak positions between the ON state and pinched OFF state at the same drain bias to measure the temperature depends upon two critical conditions: (i) the average vertical electric field in the region of interest is approximately the same in the pinched OFF state and the ON state and (ii) the total stress in the ON state can be decomposed into its components from the two effects $\sigma^{ON} = \sigma^{IPE} + \sigma^{TE}$. In

Figure 4, we demonstrated from electrical device modeling in Silvaco ATLAS/BLAZE that condition (i) is approximately true. In the following discussion, we also show that condition (ii) is approximately true under certain conditions.

In the ON state, the mechanical displacement, strain, and stress are determined by Equation (16), which we rewrite here in indicial notation for clarity

$$\frac{\partial}{\partial x_j}\sigma_{ij} = 0 \tag{B1}$$

Similarly, we can rewrite the constitutive relation in terms of the stress on the left hand side in the full tensor notation

$$\sigma_{ij} = C_{ijk\ell}\epsilon_{k\ell} - e_{kij}E_k + C_{ijk\ell}\alpha_{k\ell}\Delta T \tag{B2}$$

Inserting Equation (B2) into (B1) yields an equation for the strain with the inverse piezoelectric and thermal expansion terms written as source terms on the right hand side

$$\frac{\partial}{\partial x_j}\left(C_{ijk\ell}\epsilon_{k\ell}\right) = \frac{\partial}{\partial x_j}\left(e_{kij}E_k\right) - \frac{\partial}{\partial x_j}\left(C_{ijk\ell}\alpha_{k\ell}\Delta T\right) \tag{B3}$$

From the mechanical point of view, the electric field $\vec{E}(\vec{x})$ and temperature $T(\vec{x})$ distributions are considered as inputs obtained by solving the electrostatic and heat conduction equations, respectively, to determine the displacement $\vec{u}$, strain $\overleftrightarrow{\epsilon}$, and stress $\overleftrightarrow{\sigma}$ fields. In the most rigorous case, the electric field and temperature distributions are themselves affected by mechanical displacement, i.e., $\vec{E} = \vec{E}(\vec{x}')$ and $T = T(\vec{x}')$, where $\vec{x}' = \vec{x} + \vec{u}$ is the deformed coordinate, because deformation changes the geometry and spatial distribution of electric charge, power dissipation, *etc.* If the total strain and displacement are small such that $\vec{x}' \approx \vec{x}$, then the electric field and temperature distributions are approximately independent of strain and of each other.

Assuming that the elastic constants do not vary significantly with strain or temperature, the product $C_{ijk\ell}\epsilon_{k\ell}$ can be decomposed into a sum of products $C_{ijk\ell}\epsilon_{k\ell} = \left(C_{ijk\ell}\epsilon_{k\ell}\right)^{IPE} + \left(C_{ijk\ell}\epsilon_{k\ell}\right)^{TE}$ associated with the IPE and thermoelastic effects, respectively, and the static equilibrium condition in Equation (B3) divided into two equations

$$\frac{\partial}{\partial x_j}\left(C_{ijk\ell}\epsilon_{k\ell}\right)^{IPE} = \frac{\partial}{\partial x_j}\left(e_{kij}E_k\right) \tag{B4a}$$

$$\frac{\partial}{\partial x_j}\left(C_{ijk\ell}\epsilon_{k\ell}\right)^{TE} = -\frac{\partial}{\partial x_j}\left(C_{ijk\ell}\alpha_{k\ell}\Delta T\right) \tag{B4b}$$

The solutions for the displacement and strain distributions due to the IPE and thermoelastic effects can be computed independently by solving Equations (B4a) and (B4b) with the same mechanical boundary conditions. Combining the strain distributions from these two independent problems $\epsilon_{k\ell} = \epsilon_{k\ell}^{IPE} + \epsilon_{k\ell}^{TE}$ and Equation (B3) leads to the conclusion that $\sigma_{ij} = \sigma_{ij}^{IPE} + \sigma_{ij}^{TE}$.

References

[1]   Y.-F. Wu, M. Moore, A. Saxler, T. Wisleder and P. Parikh in *Proceedings of the 64th Device Research Conference*, State College, PA, USA 26 June-28 June 2006 (IEEE, 2006), pp. 151-152.
[2]   M. Kuball, J. M. Hayes, M. J. Uren, T. Martin, J. C. H. Birbeck, R. S. Balmer and B. T. Hughes, IEEE Electron Device Lett. **23**, 7 (2002).
[3]   M. Kuball, S. Rajasingam, A. Sarua, M. J. Uren, T. Martin, B. T. Hughes, K. P. Hilton and R. S. Balmer, Appl. Phys. Lett. **82**, 124 (2003).
[4]   A. Sarua, H. Ji, M. Kuball, M. J. Uren, T. Martin, K. P. Hilton and R. S. Balmer, IEEE Trans. Electron Devices **53**, 2438 (2006).
[5]   A. Sarua, H. Ji, K. P. Hilton, D. J. Wallis, M. J. Uren, T. Martin, and M. Kuball, IEEE Trans. Electron Devices 54, 3152 (2007).
[6]   G. J. Riedel, J. W. Pomeroy, K. P. Hilton, J. O. Maclean, D. J. Wallis, M. J. Uren, T. Martin, and M. Kuball, IEEE Electron Device Lett. **29**, 416 (2008).
[7]   T. Batten, J. W. Pomeroy, M. J. Uren, T. Martin, and M. Kuball, J. Appl. Phys. **106**, 094509 (2009).
[8]   T. Beechem, A. Christiensen, S. Graham, and D. Green, J. Appl. Phys **103**, 124501 (2008).
[9]   S. Choi, E. R. Heller, D. Dorsey, R. Vetury, and S. Graham, IEEE Trans. Electron Devices **60**, 1898 (2013).

[10] J. W. Pomeroy, M. Kuball, M. J. Uren, and T. Martin, Phys. Stat. Sol. B **245**, 910 (2008).

[11] M. S. Liu, L. A. Bursill, S. Prawer, K. W. Nugent, Y. Z. Tong and G. Y. Zhang, Appl. Phys. Lett. **74**, 3125 (1999).

[12] A. Sarua, H. Ji, M. Kuball, M. J. Uren, T. Martin, K. J. Nash, K. P. Hilton and R. S. Balmer, Appl. Phys. Lett. **88**, 103502 (2006).

[13] A. Sarua, H. Ji, J. W. Pomeroy, M. J. Uren, T. Martin and M. Kuball, Semicond. Sci. Technol. **25**, 085004 (2010).

[14] T. Beechem, A. Christensen, D. S. Green, and S. Graham, J. Appl. Phys. **106**, 114509 (2009).

[15] *The Raman Effect*, edited by A. Anderson (Marcel Dekker, New York, 1971).

[16] M. Kuball, Surf. Interface Anal. **31**, 987 (2001).

[17] C. Ulrich, E. Anastassakis, K. Syassen, A. Debernardi, and M. Cardona, Phys. Rev. Lett. **78**, 1283 (1997).

[18] Y. Liu and J. Lin, J. Opt. Soc. Am. B 18, 666 (2001).

[19] R. Quay, *Gallium Nitride Electronics* (Springer-Verlag, Berlin, 2008).

[20] O. Ambacher, J. Smart, J. R. Shealy, N. G. Weimann, K. Chu, M. Murphy, W. J. Schaff, L. F. Eastman, R. Dimitrov, L. Wittmer, M. Stutzmann, W. Rieger and J. Hilsenbeck, J. Appl. Phys. **85**, 3222 (1999).

[21] E. Zanoni, M. Meneghini, A. Chini, D. Marcon, and G. Meneghesso, IEEE Trans. Electron Devices **60**, 3119 (2013).

[22] S. Chowdhury and U. K. Mishra, IEEE Trans. Electron Devices **60**, 3060 (2013).

[23] K. Momma and F. Izumi, J. Appl. Crystallogr. **44**, 1272 (2011).

[24] S. Yoshida, S. Katoh, H. Takehara, Y. Satoh, J. Li, N. Ikeda, K. Hataya and H. Sasaki, Phys. Stat. Sol. A **7**, 1739 (2006).

[25] J. F. Nye, *Physical Properties of Crystals: Their Representation by Tensors and Matrices* (Oxford University Press, London, 1957).

[26] J. G. Brainerd et al., Proc. I.R.E., 1378 (1949).

[27] V. Darakchieva, T. Paskova, M. Schubert, H. Arwin, P. P. Paskov, B. Monemar, D. Hommel, M. Heuken, J. Off, F. Scholz, B. A. Haskell, P. T. Fini, J. S. Speck and S. Nakamura, Phys. Rev. B **75**, 195217 (2007).

[28] C. A. Arguello, D. L. Rousseau and S. P. S. Porto, Phys. Rev. **181**, 1351 (1969).

[29] N. J. Everall, Appl. Spectroscopy **63**, 245 (2009).

[30] J. B. Cui, K. Amtmann, J. Ristein, and L. Ley , J. Appl. Phys. **82**, 7929 (1998).

[31] J. M. Hayes, M. Kuball, Y. Shi and J. H. Edgar, Proc. Mat. Res. Soc. Symp. **639**, G6.38.1 (2001).

[32] J. Menendez and M. Cardona, Phys. Rev. B **29**, 2051 (1984).

[33] R. J. Briggs and A. K. Ramdas, Phys. Rev. B **13**, 5518 (1974).

[34] S. Timoshenko and J. N. Goodier, *Theory of Elasticity*, 2nd ed. (McGraw-Hill, New York, 1951), pp. 11-13, 223.

[35] M. G. Ancona, S. C. Binari, and D. J. Meyer, J. Appl. Phys. **11**, 074504 (2012).

[36] *Introduction to COMSOL Multiphysics*, Version 5.0, (COMSOL Inc., Los Angeles, 2014).

[37] P. Witczak, Z. Witczak, R. Jemielniak, M. Krysko, S. Krukowski and M. Bockowski, Semicond. Sci. Technol. **30**, 1 (2015).

[38] L. E. McNeil, M. Grimsditch, and R. H. French, J. Am. Ceram. Soc. **76**, 1132 (1993).

[39] K. Kamitani, M. Grimsditch, J. C. Nipko, C.-K. Loong, M. Okada, and I. Kimura, J. Appl. Phys. **82**, 3152 (1997).

[40] A. P. Mirogorodsky, M. B. Smirnov, E. Abdelmounim, T. Merle, and P. E. Quintard, Phys. Rev. B **52**, 3993 (1995).

[41] L. Patrick and W. J. Choyke, Phys. Rev. B **2**, 2255 (1970).

[42] T. E. Beechem, Ph.D. thesis, Georgia Institute of Technology, pp. 52-53, 62-68, 2008.

[43] S. Choi, E. Heller, D. Dorsey, R. Vetury, and S. Graham J. Appl. Phys. **113**, 093510 (2013).

[44] A. Polian, M. Grimsditch, and I. Grzegory, J. Appl. Phys. **79**, 3342 (1996).

[45] W. Soluch, E. Brzozowski, M. Lysakowska and J. Sadura, IEEE Trans. Ultrasonics Ferroelec. Freq. Control **58**, 2469 (2011).

[46] G. Callsen, J. S. Reparaz, and M. R. Wagner, R. Kirste, C. Nenstiel, A. Hoffman and M. R. Phillips, Appl. Phys. Lett. **98**, 061906 (2011).

[47] F. Bernardini and V. Fiorentini, Appl. Phys. Lett. 80, 4145 (2002).

[48] A. R. Goñi, H. Siegle, K. Syassen, C. Thomsen and J.-M. Wagner, Phys. Rev. B **64**, 035205 (2001).

[49] F. Demangeot and J. Frandon, Phys. Rev. B **69**, 155215 (2004).

[50] J.-M. Wagner and F. Bechstedt, Appl. Phys. Lett. **77**, 346 (2000).

[51] B. Jogai, J. D. Albrecht and E. Pan, J. Appl. Phys. **94**, 3984 (2003).

[52] R. Loudon, Adv. Phys. **13**, 423 (1964).

[53] G. Chen, *Nanoscale Energy Transport and Conversion*, (Oxford University Press, New York, 2005), p. 166.

[54] J. Wagner, H. Obloh, M. Kunzer, M. Maier, K. Kohler, and B. Johs, J. Appl. Phys. **89**, 2779 (2001).

[55] B. Jogai, Phys. Stat. Sol. B **241**, 952 (2004).

[56] G. F. Burkhard, E. T. Hoke, and M. D. McGehee, Adv. Mat. **22**, 3293 (2010).

[57] S. Shokhovets, R. Goldhahn, G. Gobsch, S. Piekh, R. Lantier, A. Rizzi, V. Lebedev, and W. Richter, J. Appl. Phys. **94**, 307 (2003).

[58] C. Xu, S. Wang, G. Wang, J. Liang, S. Wang, L. Bai, J. Yang, and X. Chen, J. Appl. Phys. **115**, 113501 (2014).

[59] T. Kozawa, T. Kachi, H. Kano, Y. Taga, M. Hashimoto, N. Koide, and K. Manabe, J. Appl. Phys. **75**, 1098 (1994).

[60] P. Perlin, J. Camassel, W. Knap, T. Taliercio, J. C. Chervin, T. Suski, I. Grzegory, and S. Porowski, Appl. Phys. Lett. **67**, 2524 (1995).

[61] A. Debernardi, S. Baroni and E. Molinari, Phys. Rev. Lett. **75**, 1819 (1995).

[62] J. M. Worlock and P. A. Fleury, Phys. Rev. Lett. **19**, 1176 (1967).

[63] X. Wang and D. Vanderbilt, Phys. Rev. B **74**, 054304 (2006).